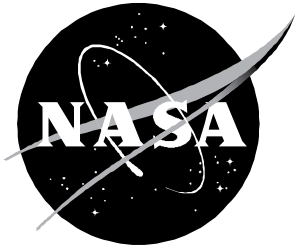


# Acoustic Receptivity Due to Weak Surface Inhomogeneities in Adverse Pressure Gradient Boundary Layers

---

*Meelan Choudhari, Lian Ng, and Craig Streett*



# Acoustic Receptivity Due to Weak Surface Inhomogeneities in Adverse Pressure Gradient Boundary Layers

---

*Meelan Choudhari*  
*High Technology Corporation • Hampton, Virginia*

*Lian Ng*  
*Analytical Services & Materials Inc. • Hampton, Virginia*

*Craig Streett*  
*Langley Research Center • Hampton, Virginia*

### **Acknowledgments**

The research of the first two authors was supported by the Theoretical Flow Physics Branch at the NASA Langley Research Center, Hampton, VA under contract numbers NAS1-18240 and NAS1-18599 and completed in 1991. The authors thank Gordon Erlebacher for his timely improvements in the graphics package GRAPHICUS, which was of great help in analyzing the various pieces of numerical data. A brief summary of the early results was also presented in reference 43.

This publication is available from the following sources:

NASA Center for Aerospace Information  
800 Elkridge Landing Road  
Linthicum Heights, MD 21090-2934  
(301) 621-0390

National Technical Information Service (NTIS)  
5285 Port Royal Road  
Springfield, VA 22161-2171  
(703) 487-4650

## Abstract

*The boundary layer receptivity to free-stream acoustic waves in the presence of localized surface disturbances is studied for the case of incompressible Falkner-Skan flows with adverse pressure gradients. These boundary layers are unstable to both viscous and inviscid (i.e., inflectional) modes, and the finite Reynolds number extension of the Goldstein-Ruban theory provides a convenient method to compare the efficiency of the localized receptivity processes in these two cases. The value of the efficiency function related to the receptivity caused by localized distortions in surface geometry is relatively insensitive to the type of instability mechanism, provided that the same reference length scale is used to normalize the efficiency function for each type of instability. In contrast, when the receptivity is induced by variations in wall suction velocity or in wall admittance distribution, the magnitudes of the related efficiency functions, as well as the resulting coupling coefficients, are smaller for inflectional (i.e., Rayleigh) modes than for the viscous Tollmien-Schlichting waves. The reduced levels of receptivity can be attributed mainly to the shorter wavelengths and higher frequencies of the inflectional modes. Because the most critical band of frequencies shifts toward higher values, the overall efficiency of the wall suction- and wall admittance-induced receptivity decreases with an increase in the adverse pressure gradient.*

## 1. Introduction

The pressure gradient in the external stream is known to exert a significant influence upon the laminar to turbulent flow transition within the boundary layer. The experiments of Schubauer and Skramstad (ref. 1), which for the first time established a firm connection between the linear stability theory and the transition process, demonstrated the strongly stabilizing and destabilizing roles of favorable and adverse pressure gradients, respectively, on the growth of small-amplitude disturbances in the boundary layer. Since then, this observation has also been confirmed by results from other experimental and theoretical investigations. Thus, to achieve reduced aircraft skin friction drag by delayed transition to turbulence, a favorable pressure gradient needs to be maintained over most of the wing surface. This observation forms the basis for the design of the natural laminar flow (NLF) wings (ref. 2), which have attained transition Reynolds numbers of up to approximately  $15 \times 10^6$  during in-flight experiments. (See ref. 3.)

Although the desired pressure distribution on an NLF wing may be maintained at close-to-design conditions, pockets of adverse pressure gradient can occur for off-design conditions such as high angles of attack. In conventional wing designs, an adverse pressure gradient region usually develops just downstream of the blunt leading edge. This region pro-

notes early transition and thereby substantially reduces the percentage of laminar flow over the wing. Moreover, the complex interaction between separation induced by adverse pressure gradients and the ensuing transition process can also have a detrimental effect on the overall performance of a low-Reynolds-number airfoil. (See ref. 4.) Even in the absence of separation, the adverse pressure gradient downstream of the blunt leading edge can substantially increase the amplitude of an instability wave. (See ref. 5.) Thus, it is vital to understand the characteristics of transition in boundary layer flows that are subject to adverse pressure gradients.

The first systematic study appears to be the works of Schlichting and Ulrich (ref. 6) and Pretsch (ref. 7), who used high-Reynolds-number asymptotics to investigate the stability of Falkner-Skan boundary layers at different values of the Hartree parameter  $\beta$ . An important characteristic of adverse pressure gradient flows ( $\beta < 0$ ) is their ability, by virtue of their inflectional profiles, to support the inviscid (i.e., Rayleigh type) instability as well as the viscous Tollmien-Schlichting (TS) modes which dominate the primary instability in a zero or favorable pressure gradient boundary layer. Inviscid instability is indicated by the nonzero asymptotes  $\alpha \rightarrow \alpha_{\text{ub},\infty}$  and  $\omega \rightarrow \omega_{\text{ub},\infty}$ , as  $R_{\delta^*} \rightarrow \infty$  along the upper branch of the neutral stability curve, while pure TS instability is indicated by the asymptotes  $\alpha \rightarrow 0$  and  $\omega \rightarrow 0$ . Here, the nondimensional instability wave

numbers  $\alpha$  and  $\alpha_{\text{ub},\infty}$ , the nondimensional frequencies  $\omega$  and  $\omega_{\text{ub},\infty}$ , and the flow Reynolds number  $R_{\delta^*}$  are defined in terms of a reference length scale corresponding to the local displacement thickness  $\delta^*$  and a velocity scale corresponding to the local free-stream velocity. The lower branch of the neutral curve still involves viscous (i.e., TS) modes with  $\alpha \rightarrow 0$  as  $R_{\delta^*} \rightarrow \infty$  similar to the class of boundary layers without any inflection points. Of course, note that the distinction between the viscous and inviscid mechanisms is asymptotic in nature and valid only in the limit of  $R_{\delta^*} \rightarrow \infty$ ; in practice, the instabilities of the boundary layer are simultaneously influenced by both of these mechanisms.

Wazzan, Okamura, and Smith (ref. 8) numerically solved the Orr-Sommerfeld (OS) eigenvalue problem for the Falkner-Skan profiles and found that high Reynolds numbers are required for the establishment of these asymptotic characteristics just referred to and hence, the practical utility of each individual asymptotic result is somewhat limited. The numerical results also demonstrated the decrease in the minimum critical Reynolds number and, more significantly, the increase in the maximum streamwise growth rate when the adverse pressure gradient strength increases. Saric and Nayfeh (ref. 9) refined the quasi-parallel predictions of Wazzan, Okamura, and Smith by using a weakly nonparallel theory and found that the corrected growth rates are somewhat greater than those based on the OS equation alone. By neglecting the small nonparallel corrections, Mack (ref. 10) used the  $e^N$  methods based on both an amplitude ratio and an amplitude density criterion to develop empirical predictions of the transition Reynolds number as a function of the pressure gradient parameter  $\beta$  and the level of turbulence in the free stream. The secondary instability of the Falkner-Skan boundary layers in the presence of finite amplitude primary instabilities was studied by Herbert and Bertolotti. (See ref. 4.) A direct numerical simulation of this same problem was developed by Kloker and Fasel (ref. 11) who found the mechanism of fundamental resonance to be stronger than the subharmonic secondary instability. Experimental studies of the linear and nonlinear stabilities of Falkner-Skan flows have recently been reported by Wubben, Passchier, and Van Ingen (ref. 12) and Watmuff (ref. 13); the results in reference 12 confirm the linear stability predictions during the early stage of the transition process. The effect of an adverse pressure gradient on the amplification of an instability wave in a more realistic configuration can also be inferred from the theoretical prediction (ref. 5) of the instability wave growth in the Leehey and Shapiro ex-

periment. (See ref. 14.) In particular, Goldstein and Hultgren (ref. 5) found that the acoustically forced instability wave was amplified by a factor of approximately 2.5 between the blunt leading-edge juncture and the measurement station compared with a predicted decay for a zero pressure gradient boundary layer.

The results of the latter two investigations (refs. 5 and 14) confirm the earlier prediction (ref. 15) that adverse pressure gradient regions in nonsimilar boundary layers were strong preamplifiers of boundary layer disturbances for the noninflected profiles farther downstream. However, the manner in which an adverse pressure gradient can affect the mechanisms by which these unstable disturbances are generated in the first place should also be examined (i.e., the receptivity stage which initiates the transition process). Morkovin (ref. 16) first recognized the importance of instability wave generation in a laminar shear flow by its disturbance environment and coined the term “receptivity” for this process. Early experimental work on the receptivity of boundary layer flow by Leehey and Shapiro (ref. 14), Kachanov, Kozlov, and Levchenko (ref. 17), and Aizin and Polyakov (ref. 18) and the numerical simulations by Murdock (ref. 19) stimulated the interest of theoreticians in explaining the physical mechanisms of boundary layer receptivity. The first significant breakthrough was provided by the work of Goldstein. (See refs. 20–22.) He showed that unsteady free-stream disturbances excite the instability modes in a boundary layer flow by a wavelength conversion process (ref. 23) that accrues from rapid mean flow variations near different types of boundary inhomogeneities. Examples include the leading-edge region (ref. 20), downstream variations in surface boundary conditions such as roughness elements (ref. 21), and a region of marginal separation that is forced by a locally adverse pressure gradient. (See ref. 22.) The acoustic receptivity caused by a localized roughness element was independently studied by Ruban (ref. 24) using high-Reynolds-number asymptotic methods similar to Goldstein. (See ref. 21.) The general features of the Goldstein-Ruban theory have since been verified with the experimental observations of Aizin and Polyakov. (See ref. 5.) The distributed receptivity caused by small-amplitude surface waviness was studied by Zavolskii et al. (ref. 25) using a finite Reynolds number approach based on the OS equation. Boundary layer receptivity is currently an active area of research, as indicated in references 26–28 and the various papers in references 29 and 30, which provide insight into the types of problems which have been solved thus far.

Because of their proximity to the region of instability amplification, short-scale variations in the surface boundary conditions constitute an important class of catalysts in the receptivity process; for example, see the comparison with leading-edge receptivity in references 5 and 21. In spite of the various forms in which these nonuniformities appear in practice (e.g., variations in surface geometry (refs. 21, 24, 25, and 31), surface suction velocity, surface admittance (refs. 32 and 33), and wall temperature (ref. 34)), the basic mechanism of the receptivity process in each case is the same as that proposed by Goldstein. Basically, the unsteady field produced by the scattering of a free-stream disturbance by a local surface inhomogeneity inherits its temporal scale from the free-stream disturbance and spatial scales from the sums and differences of all the wave numbers from the free-stream and surface disturbances; thereby, the unsteady field acquires a Fourier spectrum which overlaps that of the boundary layer instabilities.

With regard to the influence of an adverse pressure gradient on the receptivity of a boundary layer, Goldstein, Leib, and Cowley (ref. 22) showed that strongly adverse pressure gradients can provide an additional receptivity mechanism by inducing rapid mean flow variations in a local region of marginal separation. The present paper examines the role of somewhat weaker, but possibly larger scale, adverse pressure gradients as modifiers of the receptivity which is induced by short-scale inhomogeneities on the airfoil surface such as wall humps and suction slots and/or strips. More specifically, the intention is to clarify the differences between the generation of TS waves and the inflectional instabilities by this latter class of receptivity mechanisms. Attention will be focused primarily upon the receptivity caused by localized and suitably weak surface nonuniformities that involve short-scale variations in the surface suction velocity, surface admittance, or surface geometry (more detailed discussion in section 3). Variations in surface suction and surface admittance are relevant to suction surfaces that are used in laminar flow control (LFC), but irregularities in shape can be found on the surface of almost any airfoil. Because such nonuniformities can occur well downstream of the leading edge (i.e., close to the region of instability), they are particularly detrimental to maintaining laminar flow. Receptivity mechanisms related to these surface perturbations were first identified by Goldstein (ref. 21), Ruban (ref. 24), Kerschen and Choudhari (ref. 32, details in Choudhari (ref. 33)) in the context of the generation of TS instabilities; these references provide a more complete discussion

of the mechanisms by which energy is transferred to the instability wave in each case.

Although the analyses of Goldstein, Ruban, and Kerschen and Choudhari utilized the triple-deck theory, which is an asymptotic approximation of the set of Navier-Stokes equations in the infinite Reynolds number limit, the Goldstein-Ruban theory can also be generalized quite easily to finite, but moderately high, Reynolds numbers. (See ref. 28.) Such finite Reynolds number predictions have recently been presented by a number of authors, including Choudhari and Streett (ref. 35), Choudhari (refs. 36 and 37), Crouch (refs. 38 and 39), and Pal and Meyer (ref. 40). However, note that a similar and completely equivalent approach which utilized the concept of adjoint eigenfunctions was first described in the Russian literature by Fedorov (ref. 41), and Tumin and Fedorov. (See ref. 42.) The OS equation was also used by Goldstein and Hultgren (ref. 5) in the context of receptivity problems. However, they used it to predict the amplification of the generated instability wave; the receptivity was predicted by the triple-deck theory of Goldstein (ref. 21) and Ruban. (See ref. 24.) Formally, the triple-deck theory is only applicable to TS instability modes near their lower branch. However, Choudhari and Streett (ref. 35) and Choudhari, Ng, and Streett (ref. 43) have indicated that, by recasting this theory in terms of the quasi-parallel stability equations (i.e., the OS equation in the incompressible case), a wider class of boundary layer instabilities can be addressed such as the unsteady Rayleigh modes in inflectional and/or compressible two-dimensional boundary layers and crossflow vortices in three-dimensional boundary layers. Because of the presence of both TS and Rayleigh mechanisms of instability in the present problem, this finite Reynolds number adaptation seems particularly attractive for the investigation of the influence of an adverse pressure gradient on the receptivity mechanisms that are related to surface nonuniformities.

In view of the numerous stability-related investigations described previously, the receptivity study should naturally include the Falkner-Skan family of incompressible boundary layers. These self-similar profiles allow the pressure gradient to be varied in a systematic manner and can be used with the assumption of local similarity in order to predict the receptivity of a more general class of boundary layer flows (e.g., the recent work of Jiang and Gaster (ref. 44), which demonstrates that the stability of arbitrary nonsimilar boundary layers can be predicted with impressive accuracy by using the local similarity principle). This paper concentrates primarily on

acoustic free-stream disturbances because, in low-speed flows, the receptivity to acoustic disturbances is an order of magnitude greater than the receptivity to convected vortical disturbances. (See ref. 28.) This result was originally established for the viscous TS modes only; however, when based on a qualitative comparison of the respective signatures within the boundary layer, the above conclusion is expected to hold in the case of Rayleigh modes as well.

The topics of the remaining part of the paper are as follows. In section 3, the finite Reynolds number approach is applied to boundary layers with nonzero pressure gradients. A detailed set of numerical results, which expands on the results presented in reference 43, and a discussion of the differences between the receptivity characteristics in the viscous (TS) and inviscid (i.e., inflectional or Rayleigh) regimes are presented in section 4.

## 2. Symbols

An asterisk (\*) indicates a dimensional quantity, a superscript bar ( $\bar{\phantom{x}}$ ) denotes the Fourier transform in the streamwise direction, and a caret ( $\hat{\phantom{x}}$ ) indicates the profile of a slowly varying quantity at the location of the surface nonuniformity.

$C_u$	local coupling coefficient based on maximum streamwise velocity fluctuation across boundary layer	$t$	nondimensional time, $\frac{U_\infty^* t^*}{L^*}$
$D$	differentiation operator along wall-normal ( $Y$ ) direction	$U^{(j)}$	perturbation to mean streamwise velocity because of stationary surface nonuniformity of type $j$
$D_\alpha$	desynchronization factor	$U_\infty^*$	free-stream velocity at reference location
$\tilde{D}_\alpha$	quantity related to desynchronization factor	$u^*$	unsteady perturbation to streamwise velocity
$E$	eigenfunction for instability wave	$V^{(j)}$	perturbation to mean surface-normal velocity because of stationary surface nonuniformity of type $j$
$F^{(j)}$	spatial distribution of surface nonuniformity of type $j$	$v$	unsteady perturbation to surface-normal velocity
$f$	nondimensional frequency parameter, $\frac{\omega^* \nu_\infty^*}{U_\infty^{*2}}$	$X$	local streamwise coordinate, $\frac{x^*}{L^*}$
$f_{FS}$	Falkner-Skan stream function, (eqs. (3.2))	$x$	slow streamwise coordinate, $\frac{x^*}{\ell^*}$
$L^*$	streamwise length scale of surface nonuniformity (associated with $\delta^*$ for computational convenience)	$x^*$	dimensional coordinate in streamwise direction
$\ell^*$	distance from leading edge to surface nonuniformity	$Y$	nondimensional surface-normal coordinate, $\frac{y^*}{L^*}$
$R$	Reynolds number based on free-stream velocity $U_\infty^*$ at reference location	$y^*$	dimensional coordinate in surface-normal direction
		$\alpha$	streamwise wave number nondimensionalized by $\delta^*$
		$\beta$	pressure gradient parameter (i.e., Hartree) in Falkner-Skan solution, (eqs. (3.2))
		$\delta^*$	local displacement thickness of mean boundary layer
		$\epsilon$	small parameter in perturbation series
		$\eta$	Falkner-Skan similarity coordinate, $y^* \sqrt{\frac{U_e^*(x^*)}{(2-\beta)\nu^* x^*}}$
		$\Lambda_u^{(j)}$	efficiency function based on amplitude of streamwise velocity fluctuation associated with generated instability wave for surface nonuniformity of type $j$
		$\nu^*$	kinematic viscosity of fluid
		$\Psi$	steady stream function
		$\psi$	unsteady perturbation to stream function
		$\omega$	nondimensional local frequency, $\frac{\omega^* L^*}{U_\infty^*}$
		Subscripts:	
		ac	acoustic (disturbance)

$e$	local inviscid free stream
fs	free stream (disturbance)
ins	instability wave
lb	lower branch of neutral stability curve
mg	maximum spatial growth rate, location or frequency
ub	upper branch of neutral stability curve
ub, $\infty$	upper branch asymptote as $R_{\delta^*} \rightarrow \infty$
$w$	wall (disturbance)
0	zeroth-order solution for steady or unsteady part of stream function
1	first-order perturbation to steady or unsteady part of stream function
$\delta^*$	based on local displacement thickness of mean boundary layer
Superscripts:	
( $j$ )	type of surface nonuniformity: $j = 1$ for wall suction variation $j = 2$ for wall admittance variation $j = 3$ for wall geometry variation

Abbreviations:

FS	Falkner-Skan
LFC	laminar flow control
NLF	natural laminar flow
OS	Orr-Sommerfeld
TS	Tollmien-Schlichting

### 3. Summary of Finite Reynolds Number Approach

The following discussion summarizes the application of the finite Reynolds number approach to receptivity of adverse pressure gradient Falkner-Skan boundary layers. As previously mentioned, a complete description of the issues underlying a localized receptivity theory has been given by Goldstein in his pioneering work (ref. 21), and the modifications involved in a finite Reynolds number approach are discussed in detail in references 36–39. The latter papers, in particular reference 36, provide detailed comparisons of the finite Reynolds number predictions with those based on Goldstein-Ruban theory as well as with the recent experimental data of Saric, Hoos, and Radeztsky. (See ref. 45.) For completeness, the principal ideas of the finite Reynolds number approach are reiterated in this paper.

Consider the flow past a semi-infinite flat surface which is inclined at an angle  $\beta\pi/2$  to the incoming stream. (See fig. 1.) Negative values of  $\beta$  correspond to positive angles of attack and, therefore, to a decreasing slip velocity

$$U_e^*(x^*) = U_\infty^* x^{\beta/(2-\beta)} \quad (3.1)$$

on the upper surface, where  $x = x^*/\ell^*$  denotes the distance from the leading edge, nondimensionalized with respect to some reference length  $\ell^*$  (identified later with the position of the surface inhomogeneity), and  $U_\infty^*$  is the free-stream velocity at the reference location  $x^* = \ell^*$ . The boundary layer flow, which develops under the adverse pressure gradient corresponding to equation (3.1), is described by the self-similar stream function

$$\left. \begin{aligned} \Psi_0^*(x^*, y^*) &= \sqrt{(2-\beta)U_e^*(x^*)\nu^*x^*} f_{\text{FS}}(\eta) \\ \eta &= y^* \sqrt{\frac{U_e^*(x^*)}{(2-\beta)\nu^*x^*}} \end{aligned} \right\} \quad (3.2a)$$

where  $y^*$  is the coordinate normal to the surface,  $\nu^*$  is the kinematic viscosity of the fluid, and  $f_{\text{FS}}(\eta)$  satisfies

$$\left. \begin{aligned} f_{\text{FS}}''' + f_{\text{FS}} f_{\text{FS}}'' + \beta(1 - f_{\text{FS}}^2) &= 0 \\ f_{\text{FS}}(0) = f_{\text{FS}}'(0) = 0 \quad f_{\text{FS}}'(\infty) &= 1 \end{aligned} \right\} \quad (3.2b)$$

The cause of receptivity is assumed to be a local nonuniformity of length scale  $L^*$  on the surface at a distance  $\ell^*$  ( $\ell^* \gg L^*$ ) downstream of the leading edge. (See fig. 1.) In particular, the receptivity produced by small but rapid changes in the mean suction-blowing velocity, the surface admittance, or the geometry of the surface will be considered. A porous surface of nonzero admittance essentially sets up an unsteady mass flux through the suction holes when the surface pressure fluctuates as a result of an incident acoustic wave. Therefore, direct specification of the distribution of this unsteady mass flux is more convenient than its computation from the surface admittance distribution. Accordingly, without any loss of generality, the streamwise distributions of the mean suction-blowing velocity, the unsteady normal velocity, and the surface height above its nominal position are assumed to be given by  $\epsilon_w^{(1)} U_\infty^* F^{(1)}(X)$ ,  $\epsilon_w^{(2)} u_{\text{ac}}^* F^{(2)}(X)$ , and  $\epsilon_w^{(3)} L^* F^{(3)}(X)$ , respectively; the small parameters  $\epsilon_w^{(j)}$  ( $j = 1, 2, 3$ ) indicate the amplitude of the local variation scaled by the appropriate reference quantities indicated by asterisks, and functions  $F^{(j)}(X)$  characterize the

geometry of the variation in terms of the local coordinate  $X = (x^* - \ell^*)/L^*$ . Note that to provide the necessary coupling between the free-stream disturbance and the instability wave, the surface disturbance length scale  $L^*$  must be of the same order of magnitude as the local instability wavelength at the frequency under consideration. (See refs. 21 and 24.)

The unsteady perturbation in the free stream is assumed to be a low-amplitude acoustic disturbance propagating parallel to the incoming stream and varying harmonically in time at a frequency  $\omega^*$ . Because the acoustic wavelength is infinite in the low-Mach-number limit, the outer unsteady motion is simply a temporal modulation of the local mean flow, and the unsteady slip velocity field is then given by

$$u_e^*(x^*) = u_{ac}^* x^{\beta/(2-\beta)} e^{-i\omega^* t^*} \quad (3.3)$$

where  $u_{ac}^*$  denotes the magnitude of the unsteady slip velocity at the surface inhomogeneity location such that  $\epsilon_{fs} \equiv u_{ac}^*/U_\infty^* \ll 1$ .

By exploiting the presence of the two small amplitude parameters  $\epsilon_w$  and  $\epsilon_{fs}$  in the problem, the local motion near the surface inhomogeneity can be expanded in terms of the dual perturbation series

$$\begin{aligned} \psi^{(j)} &= \Psi_0(x, Y) + \epsilon_w^{(j)} \Psi_1^{(j)}(X, Y) \\ &+ \epsilon_{fs} \psi_0(x, Y) e^{-i\omega t} + \epsilon_{fs} \epsilon_w^{(j)} \psi_1^{(j)}(X, Y) e^{-i\omega t} \\ &+ O\left\{ \epsilon_{fs}^2, \left[ \epsilon_w^{(j)} \right]^2 \right\} \end{aligned} \quad (3.4)$$

where the stream function  $\psi^{(j)}$  ( $j = 1, 2, 3$ ), wall-normal coordinate  $Y$ , nondimensional acoustic frequency  $\omega$ , and time  $t$  have been nondimensionalized by  $U_\infty^* L^*$ ,  $L^*$ ,  $U_\infty^*/L^*$ , and  $L^*/U_\infty^*$ , respectively. Note that, even though the instability wavelength  $L^*$  varies by an order of magnitude through the frequency range of interest,  $L^*$  will henceforth be associated with the local displacement thickness  $\delta^*$  for computational convenience.

Observe that the streamwise dependence of each term in equation (3.4) is indicated by either the local  $X$  or the global  $x$  coordinate. Each term in the perturbation expansion then represents a unique combination of spatial and temporal scales that is associated with the physical origin of that term. Briefly, the zeroth-order term  $\Psi_0(x, Y)$  corresponds to the unperturbed base flow (i.e., the mean boundary layer motion in the absence of any perturbations) which depends only on the global streamwise coordinate  $x$ . The first-order perturbations  $\Psi_1^{(1)}$  and  $\psi_0$

represent the steady but local and unsteady but slowly varying signatures, on the above base flow, induced by the surface inhomogeneity and the free-stream acoustic wave, respectively. The first term that exhibits unsteadiness as well as fast streamwise dependence and is, therefore, relevant to the generation of instability waves corresponds to the  $O\left[\epsilon_{fs} \epsilon_w^{(j)}\right]$  term produced by the mutual interaction of the two first-order perturbations. In the case of the wall admittance problem, the short-scale unsteady field  $\psi_1^{(2)}$  is produced directly by the interaction of the  $O(\epsilon_{fs})$  free-stream disturbance with the  $O\left[\epsilon_w^{(2)}\right]$  wall admittance. Because none of the other quadratic terms (i.e.,  $O\left(\epsilon_{fs}^2\right)$  and  $O\left[\epsilon_w^{(j)}\right]^2$ ) produced by the self-interaction of the two first-order perturbations possesses the desired combination of spatio-temporal scales, the receptivity problem reduces to solving for the stream function  $\psi_1^{(j)}(X, Y)$  and/or extracting the part that corresponds to the unstable mode.

An asymptotic approach would involve a further expansion (singular perturbation) of each term in equation (3.4) in terms of inverse powers (and sometimes logarithms) of the Reynolds number  $R_{\delta^*}$ . If the interest is limited to the zeroth-order solution for the instability wave amplitude, then the computation of just the leading term in each of the above expansions in terms of  $R_{\delta^*}$  is sufficient. Thus, the steady base flow  $\Psi_0(x, Y)$  is given by the non-dimensional form of the Falkner-Skan stream function. (See eqs. (3.2a) and (3.2b).) In most stability applications, usually  $\omega \ll R_{\delta^*}$ ; hence, the acoustic signature field  $\psi_0(x, Y)$  is governed by the linearized form of the unsteady boundary layer equation. Whenever  $\omega$  satisfies the stronger constraint of  $1/R_{\delta^*} \ll \omega \ll R_{\delta^*}$ ,  $\psi_0(x, Y)$  is given by the Stokes shear wave to the leading order; the higher order terms can be obtained in the manner described by Ackerberg and Phillips (ref. 46) and Goldstein, Sockol, and Sanz (ref. 47), who studied the zero pressure gradient case (i.e.,  $\beta = 0.0$  in eq. (3.1)). In general, the latter constraint is satisfied for both TS and Rayleigh modes. However, as the results of section 4.1 show, an exception is encountered when  $\beta = -0.1988$  (i.e., the separation profile case) wherein  $\omega \ll 1/R_{\delta^*}$  along the lower branch. The acoustic signature  $\psi_0(x, Y)$  is quasi-steady in this particular case. The complexity arises in the calculation of the short-scale perturbations  $\Psi_1^{(j)}(X, Y)$  and, especially, of  $\psi_1^{(j)}(X, Y)$ , which can have different asymptotic structures that depend on the particular

streamwise length scale and/or frequency. For length scales that are relevant to the generation of instability modes in the vicinity of the lower branch of the neutral stability curve, the mean flow perturbations  $\Psi_1^{(1)}$  and  $\Psi_1^{(3)}$  satisfy the steady and linearized triple-deck (i.e., interactive boundary layer) equations. However, at larger wave numbers, these perturbations are governed by a noninteractive structure described by Smith et al. (See ref. 48.) Similarly, the unsteady short-scale field  $\psi_1^{(j)}(X, Y)$  is governed by a linearized but inhomogeneous form of either the unsteady triple-deck equations (ref. 49), quintuple-deck equations (ref. 50), or a Rayleigh equation (possibly inhomogeneous) supplemented by the inhomogeneous viscous equations for the region close to the wall and in the critical layer; the choice depends on the relative scaling of the frequency parameter  $\omega$  and the local Reynolds number  $R_{\delta^*}$ .

An alternate path, which is similar to that taken in the conventional studies of boundary layer stability (refs. 8 and 10 quoted earlier) and in some recent studies of the receptivity phenomenon (refs. 35–41), exploits the well-known disparity between the length scales  $\ell^*$  and  $L^*$  of the base flow and the instability wave, respectively, at sufficiently high values of the Reynolds number  $R_{\delta^*}$ ; at the same time, the method treats  $R_{\delta^*}$  as a finite quantity in order to obtain a single set of operators that will be valid in all asymptotic regions, at least, to the leading order of approximation. Thus, by neglecting the streamwise variations of the quantities  $\Psi_0(x, Y)$  and  $\psi_0(x, Y)$ , which depend only on the global streamwise coordinate  $x$ , their respective profiles may effectively be frozen at the wall inhomogeneity location  $x = 1$ . The Stokes wave solution mentioned in the previous paragraph turns out to be a convenient approximation for  $\psi_0(x, Y)$  in the finite Reynolds number approach (refs. 36 and 37) except in the low-Strouhal-number region ( $\omega R_{\delta^*} \leq O(1)$ ) encountered at  $\beta = -0.1988$  as discussed before. Both the mean and unsteady short-scale perturbations  $\Psi_1^{(j)}$  and  $\psi_1^{(j)}$  then satisfy the usual equations of parallel flow disturbance, which reduce to the Orr-Sommerfeld (OS) equation in the Fourier transform space. (See refs. 36 and 37.)

Accordingly, Fourier transforms of the steady perturbations  $\bar{\Psi}_1^{(1)}$  and  $\bar{\Psi}_1^{(3)}$  are governed by the time-independent form of the Orr-Sommerfeld equation

$$i\alpha \hat{\Psi}'_0 (D^2 - \alpha^2) \bar{\Psi}_1^{(j)} - i\alpha \hat{\Psi}'''_0 \bar{\Psi}_1^{(j)} - \frac{1}{R_{\delta^*}} (D^2 - \alpha^2)^2 \bar{\Psi}_1^{(j)} = 0 \quad (j = 1, 3) \quad (3.5a)$$

subject to an inhomogeneous boundary condition that corresponds to a specified distribution of the wall suction velocity

$$\bar{\Psi}_1^{(1)}(0) = \frac{\bar{F}^{(1)}(\alpha)}{i\alpha} \quad (3.5b)$$

or to a nonzero horizontal velocity

$$D\bar{\Psi}_1^{(3)}(0) = -\hat{\Psi}''_0(0) \bar{F}^{(3)}(\alpha) \quad (3.5c)$$

Note that the boundary condition (eq. (3.5c)) arises from the transfer of the no-slip condition from the deformed surface position  $Y = \epsilon_w^{(3)} F^{(3)}(X)$  to its unperturbed location  $Y = 0$ . The caret on  $\hat{\Psi}_0$  in equation (3.5a) and on  $\hat{\psi}_0$  in equation (3.6a) below represents the profile of the respective stream function quantity along the wall-normal direction at  $x = 1$ ; the operator  $D$  and the primes denote differentiation with respect to the wall-normal  $Y$  coordinate.

The unsteady scattered field  $\psi_1^{(j)}$  satisfies the inhomogeneous OS equation

$$\begin{aligned} & -i\omega(D^2 - \alpha^2) \bar{\psi}_1^{(j)} + i\alpha \hat{\Psi}'_0 (D^2 - \alpha^2) \bar{\psi}_1^{(j)} \\ & - i\alpha \hat{\Psi}'''_0 \bar{\psi}_1^{(j)} - \frac{1}{R_{\delta^*}} (D^2 - \alpha^2)^2 \bar{\psi}_1^{(j)} \\ & = -i\alpha \left[ \hat{\psi}'_0 (D^2 - \alpha^2) \bar{\Psi}_1^{(j)} - \hat{\psi}'''_0 \bar{\Psi}_1^{(j)} \right] \end{aligned} \quad (3.6a)$$

The inhomogeneous term on the right side of equation (3.6a) for  $j = 1$  and  $j = 3$  arises from a temporal modulation of the short-scale mean flow perturbation  $\Psi_1^{(j)}$  by the acoustic signature  $\psi_1^{(j)}$ . (See ref. 28.) In addition to the inhomogeneity in the differential equation itself,  $\bar{\psi}_1^{(3)}$  also satisfies the inhomogeneous boundary condition

$$D\bar{\psi}_1^{(3)}(0) = -\hat{\psi}''_0(0) \bar{F}^{(3)}(\alpha) \quad (3.6b)$$

that corresponds to a transfer of the no-slip condition for the unsteady motion. Because changes in wall admittance do not affect the mean flow,  $\Psi_1^{(2)} \equiv 0$ , and consequently, the forcing term on the right side of equation (3.6a) is equal to zero for  $j = 2$ . Thus, unlike  $\bar{\psi}_1^{(1)}$  and  $\bar{\psi}_1^{(3)}$ , the stream function  $\bar{\psi}_1^{(2)}$  for the wall admittance case satisfies a homogeneous OS equation. The motion corresponding to  $\bar{\psi}_1^{(2)}$  is directly driven by the unsteady velocity, which is

induced by the acoustic pressure fluctuations across the porous surface and is specified to be of the form

$$\bar{v}_1^{(2)}(0) = -i\alpha\bar{\psi}_1^{(2)}(0) = -\bar{F}^{(2)}(\alpha) \quad (3.6c)$$

Other than for equations (3.6b) and (3.6c), all of the other boundary conditions on  $\bar{\psi}_1^{(j)}$  ( $j = 1, 2, 3$ ) are homogeneous in character.

The physical stream function  $\psi_1^{(j)}$  can be obtained by evaluating the inverse Fourier integral

$$\psi_1^{(j)}(X, Y) = \frac{1}{\sqrt{2\pi}} \int_{-\infty}^{\infty} e^{i\alpha X} \bar{\psi}_1^{(j)}(\alpha, Y) d\alpha \quad (3.7)$$

However, the extraction of just that part of  $\psi_1^{(j)}$  that corresponds to the unstable TS wave is sufficient. This part can be computed as the residue contribution to the inverse Fourier integral in equation (3.7) from a pole singularity in  $\bar{\psi}_1^{(j)}(\alpha)$  at the wave number  $\alpha_{\text{ins}}$  that corresponds to the aforementioned unstable mode. (See refs. 21, 36, and 37.) Thus,

$$\psi_{1 \text{ ins}}^{(j)}(X, Y) = \frac{\sqrt{2\pi} i}{\left\{ \frac{\partial [\bar{\psi}_1^{(j)}]^{-1}}{\partial \alpha} \right\} \alpha = \alpha_{\text{ins}}} e^{i\alpha_{\text{ins}} X} \quad (3.8)$$

Note that the OS eigenvalue problem also admits a number of other higher modes; however, these modes are stable and, therefore, will not be considered in the present analysis. After utilizing the linear dependence of  $\bar{\psi}_1^{(j)}$  on  $\bar{F}^{(j)}$ , equation (3.8) leads to the following expression in dimensional form for the streamwise velocity fluctuation associated with the generated instability wave (refs. 21, 36, and 37):

$$u_{\text{ins}}^{*(j)}(X, Y, t) = C_u^{(j)} u_{\text{ac}}^* E_u(Y, \omega, R_{\delta^*}) e^{i(\alpha_{\text{ins}} X - \omega t)} \quad (3.9a)$$

where

$$C_u^{(j)} = \epsilon_w^{(j)} \bar{F}^{(j)}(\alpha_{\text{ins}}) \Lambda_u^{(j)}(\omega, R_{\delta^*}) \quad (3.9b)$$

and  $E_u(Y, \omega, R_{\delta^*})$  is the local instability eigenfunction for the streamwise velocity perturbation, which is normalized to have a maximum magnitude of unity across the boundary layer. The factor  $C_u^{(j)}$ , which is referred to as the ‘‘local coupling coefficient’’ (refs. 21 and 51), is essentially the transfer function that relates the output of receptivity (i.e., the local amplitude at  $X = 0$  of the generated instability wave) to its input (i.e., the local amplitude of the free-stream

acoustic disturbance). For the weak surface inhomogeneities considered here,  $C_u^{(j)}$  is linear in the amplitude of the inhomogeneity and, as seen from equation (3.9b), can be written in terms of the product of a geometry factor  $\bar{F}^{(j)}(\alpha_{\text{ins}})$  and an efficiency function  $\Lambda_u^{(j)}$ . The geometry factor corresponds to the Fourier transform of the spatial distribution of the wall inhomogeneity at the complex instability wave number  $\alpha_{\text{ins}}$ . Conversely, the efficiency function  $\Lambda_u^{(j)}$  is independent of the details of the surface inhomogeneity and, hence, characterizes the local efficiency of the receptivity process that results from an interaction between the particular surface and free-stream perturbations being considered. Because the geometry factor is common to all three combinations of the perturbations considered in this paper, the characteristics of the receptivity process in each case may be gleaned from examination of the variation of the efficiency function  $\Lambda_u^{(j)}$  with respect to both the position  $R_{\delta^*}$  of the surface nonuniformity and the frequency  $\omega$  of the acoustic disturbance.

Note that the result of equation (3.9b) is valid for all receptivity mechanisms involving weak surface inhomogeneities irrespective of the type of methodology (asymptotic or finite Reynolds number) used to solve the problem. Individually, the values of  $\bar{F}^{(j)}$  and  $\Lambda_u^{(j)}$  depend on the choice of the reference length scale in the problem; however, their product (i.e., the coupling coefficient  $C_u^{(j)}$ ) does not. In this paper, the local displacement thickness of the unperturbed mean boundary layer was chosen as the reference length scale (i.e.,  $L^* = \delta^*$ ). However, a more appropriate choice for the reference length scale might well have been the local length scale of the generated instability wave (i.e.,  $L^* = \delta^*/\alpha_{\text{ins}}$ ). Had the latter choice been made, the geometry factor  $\bar{F}^{(j)}$  and the efficiency function  $\Lambda_u^{(j)}$  in equation (3.9b) would be multiplied by  $\alpha_{\text{ins}}$  and  $1/\alpha_{\text{ins}}$ , respectively, for both  $j = 1$  and  $j = 2$ . The corresponding conversion factors for the wall geometry-induced receptivity ( $j = 3$ ) would be  $\alpha_{\text{ins}}$  and  $1/\alpha_{\text{ins}}^2$ , the latter term being different than that for the cases of  $j = 1$  and  $j = 2$  to compensate for the additional length scale dependence in the definition of the normalized height perturbation  $\epsilon_w^{(3)}$ . To maintain consistency with the previous investigations (refs. 21, 36, and 37) as well as to conform with the general practice of using a boundary layer thickness as the reference length scale in most practical applications,  $\delta^*$  was adopted as the uniform length scale at all values of the acoustic frequency parameter. However, keep in mind the aforementioned

dependence of the efficiency function values on the choice of  $\ell^*$  when interpreting the numerical results presented in the next section.

## 4. Results

As mentioned in section 1, boundary layers developing under an adverse pressure gradient can support both viscous (TS) and inviscid (inflectional, or Rayleigh) instabilities. Because the viscous modes occupy the lower branch region of the neutral stability curve, their generation can have a greater impact on the transition process. However, the critical Reynolds numbers decrease rapidly as the adverse pressure gradient increases, and consequently, the generation of inflectional modes becomes increasingly more relevant. Thus, the basic objectives of the parametric study are to understand how the coupling coefficients related to TS-mode generation are affected by the adverse pressure gradient, to assess the major differences between the receptivity characteristics in the TS and inflectional-mode regimes, and to ascertain the cause of these differences.

To meet these objectives, the stability characteristics of the Falkner-Skan boundary layers with  $\beta < 0$  will first be examined. In addition to providing a background for the later discussion on receptivity, this section will generally emphasize the importance of finite Reynolds number effects. Results that pertain to the mean flow perturbations produced by variations in the wall suction velocity or the wall geometry will subsequently be described. As discussed in section 3, these mean flow perturbations provide the spatial modulation required for generation of instability waves; their properties in adverse pressure gradient flows will be examined. Finally, the results on receptivity will be presented, and the dependence of the efficiency function  $\Lambda_u^{(j)}$  on frequency, Reynolds number, and pressure gradient parameter will be explored in detail.

### 4.1. Stability Characteristics Under Adverse Pressure Gradients

Figure 2 shows the streamwise growth rate  $-\text{Im}(\alpha_{\text{ins}})$  of the instability wave as a function of the local Strouhal number  $\omega$  for  $\beta = -0.05, -0.10, -0.14$ , and  $-0.1988$ . For each value of the pressure gradient parameter, the growth rate variations are displayed for Reynolds numbers ranging from low (for which the finite Reynolds number effects cannot be neglected) to high (which may not be very relevant from a practical point of view, because the flow may already be turbulent, but which are more representative of the inviscid asymptote for inflectional modes). Recall that the viscous and the inviscid modes are

not clearly identified at any finite Reynolds number. However, because the inviscid upper branch scaling corresponds to frequencies that are much higher than those of the lower branch ones, most of the unstable region can be expected to be basically dominated by the inflectional mechanism, especially at sufficiently high values of  $|\beta|$  and/or  $R_{\delta^*}$ .

The dominance of the inviscid mode can be gauged by whether the upper branch neutral frequency has become largely insensitive to changes in the local Reynolds number. Thus, figure 2(a) suggests that, for  $\beta = -0.05$ , viscous effects are still significant at  $R_{\delta^*} = 2000$ . However, figures 2(b)–2(d) show that for stronger pressure gradients, the inviscid neutral asymptote is nearly established at  $R_{\delta^*} = 2000$ . The maximum growth rate at these locations as well as the corresponding Strouhal number  $\omega_{\text{mg}}$  still depends on  $R_{\delta^*}$  to a significant extent. The reason for this dependence may be that the most unstable frequency  $\omega_{\text{mg}}$  lies in the viscous regime or in the domain of overlap of the viscous and the inviscid Rayleigh regimes.

Because the lower branch corresponds to predominantly viscous modes, the associated neutral frequency  $\omega_{\text{lb}}$  is dependent on the Reynolds number  $R_{\delta^*}$  at all values of  $\beta$ . However, one characteristic of the viscous TS modes becomes apparent when the lower branch frequencies are plotted against the Reynolds number on a logarithmic plot. (See fig. 3.) Slopes of the curves in figure 3 show that, for all pressure gradients other than the separation case ( $\beta = -0.1988$ ),  $\omega_{\text{lb}} \approx R_{\delta^*}^{-1/2}$  for all sufficiently large  $R_{\delta^*}$ , which corresponds to the regular triple-deck scalings. However, figure 3 indicates that, for  $\beta = -0.1988$ ,  $\omega_{\text{lb}}$  decreases faster than  $R_{\delta^*}^{-1}$ , which implies that the lower branch modes are quasi-steady. In spite of this increase in the temporal scale, the streamwise wavelengths of these instability modes remain sufficiently short for them to still be classified as parallel flow instabilities to the leading order. Indeed, Okamura, Smith, and Wazzan (ref. 52) had found numerically that the neutral wave number  $\alpha_{\text{lb}}$  varies as  $R_{\delta^*}^{-0.699}$  as  $R_{\delta^*} \rightarrow \infty$  at  $\beta = -0.1988$ , which was quite different from the scaling derived analytically by Hughes and Reid (ref. 53) for the corresponding approximate Pohlhausen profile. The validity of the quasi-parallel approximation in this paper implies that the receptivity theory from section 3 can still be used to predict the coupling coefficients but only after the high-frequency Stokes wave approximation for the acoustic signature field ( $\psi_0$ ) is replaced by its quasi-steady counterpart because of the frequency scaling ( $\omega \ll 1/R_{\delta^*}$ ) along the lower branch asymptote. Because  $\omega$  varies continuously from this

quasi-steady asymptote to  $O(1)$  values along the upper branch, the point where the Stokes wave approximation for  $\psi_0$  becomes reasonable as  $\omega$  is increased at a given Reynolds number is not easily determined. In the intermediate range of  $\omega = O(1/R_{\delta^*})$ ,  $\psi_0$  is governed by the unsteady linearized boundary layer equations (refs. 20 and 46) and, therefore, has a nontrivial dependence on the entire history of the upstream disturbance. To avoid the associated complications, the Stokes wave approximation was used for  $\psi_0$  throughout the calculations. Therefore, the receptivity results are of questionable validity in a narrow range of the frequency-Reynolds-number space when  $\beta \rightarrow -0.1988$ . However, this is of minor significance overall because the viscous instabilities are relatively unimportant in the transition of the near-separation profile. Moreover, the calculations of references 46 and 47 suggest that the Stokes wave solution may be established at frequencies close to  $\omega = O(1/R_{\delta^*})$ , i.e., well before the  $\omega \gg 1/R_{\delta^*}$  asymptotic limit is reached. Thus, in a practical sense the Stokes wave approximation is likely to provide most of the significant information concerning the receptivity of a near-separation flow.

#### 4.2. Characteristics of Mean Flow Perturbations Produced by Variations in Wall Suction and Wall Geometry

The characteristics of the mean flow perturbations produced by wall suction and wall geometry variations under adverse pressure gradient conditions will be investigated next; recall that the receptivity through the wall suction and wall geometry variations is determined entirely and in part, respectively, by the scattering of the Stokes shear wave because of the corresponding mean flow perturbation. As described in section 3, the amplitude of the generated instability wave is determined as the residue of the inverse Fourier integral for  $\psi_1^{(j)}$  because of the first-order pole singularity of  $\bar{\psi}_1^{(j)}$  at the instability wave number  $\alpha_{\text{ins}}$ . Accordingly, this is the only wave number component of the mean flow perturbation that has any significance from the standpoint of receptivity. Because the imaginary part of  $\alpha_{\text{ins}}$  is usually small when compared with its real part, the Fourier component of the mean flow perturbation corresponding to  $\alpha_{\text{ins}}$  can be approximately associated with the local flow response to sinusoidal distributions of the wall suction velocity or waviness (wall roughness) height with a wave number equal to the real part of  $\alpha_{\text{ins}}$ . The mean flow modification because of waviness of the airfoil surface or by suction through regularly spaced suction strips is a problem of significant practical importance; hence, the vari-

ous aspects of the mean flow perturbations for the specific case of  $\beta = -0.14$  will be detailed.

First, consider the mean flow perturbations  $\bar{U}_1^{(1)}$ ,  $\bar{V}_1^{(1)}$ , and  $\bar{P}_1^{(1)}$  that are produced by the wave number component  $\alpha = \alpha_{\text{ins}}$  of the wall suction distribution. Figures 4 and 5 are plots of the profiles of the magnitudes of vertical  $\bar{V}_1^{(1)}$  and streamwise  $\bar{U}_1^{(1)}$  velocity perturbations, respectively, at  $\beta = -0.14$ . Figures 4(a) and 5(a) illustrate the profiles at a Reynolds number of  $R_{\delta^*} = 500$  and figures 4(b) and 5(b) at  $R_{\delta^*} = 5000$ . The four curves in each of figures 4(a), 4(b), 5(a), and 5(b) are associated with the local instability wave number at frequencies equal to  $\omega_{\text{lb}}/2$ ,  $\omega_{\text{lb}}$ ,  $\omega_{\text{mg}}$ , and  $\omega_{\text{ub}}$  at the Reynolds number under consideration; the subscripts lb, ub, and mg refer to the lower branch, upper branch, and the maximum growth rate, respectively. The wall-normal location that corresponds to the critical layer of the instability wave at each frequency is also indicated by an  $\times$  on each of these curves. Recall that, as  $\omega$  varies from its lowest ( $\omega_{\text{lb}}/2$ ) to its highest ( $\omega_{\text{ub}}$ ) value in figures 4 and 5, the wavelength of the instability wave and, hence, that of the surface disturbance, decreases from the value of the longer triple-deck scale to a value comparable with the thickness of the boundary layer. A detailed account of the influence of the length scale of a surface disturbance based on the higher Reynolds number asymptotic theory was given by Smith et al. (ref. 48) for problems involving two-dimensional obstacles on the airfoil surface. Their analysis will be used to interpret the numerical results presented in this section.

As a result of the reduction in instability wavelength with an increase in value of the frequency parameter, the mean-flow perturbation also changes in character from interactive to that driven by a viscous layer close to the wall. This difference is reflected in the shapes of the  $|\bar{V}_1^{(1)}|$  profiles across the boundary layer. (See fig. 4.) Thus, at  $\omega = \omega_{\text{lb}}/2$  and  $\omega = \omega_{\text{lb}}$ , the unit normal velocity perturbation at the surface gets amplified considerably across the main part of the boundary layer before beginning to decay outside of the boundary layer region. In accordance with interactive (i.e., triple-deck) scaling, the extent of this amplification is also seen to increase with an increase in the Reynolds number. However, for suction distributions with shorter wavelengths corresponding to  $\omega = \omega_{\text{mg}}$  and  $\omega = \omega_{\text{ub}}$ , the resultant  $|\bar{V}_1^{(1)}|$  perturbation reaches a maximum at the surface itself and decreases nearly monotonically into the boundary layer region.

Unlike the profiles of the  $|\overline{V}_1^{(1)}|$  perturbations, profiles of the corresponding streamwise velocity perturbations  $|\overline{U}_1^{(1)}|$  are qualitatively similar for all wave numbers except  $\alpha = \alpha_{\text{mg}}$  for which the  $|\overline{U}_1^{(1)}|$  profile has three peaks rather than two as in all other cases. (See fig. 5(a).) However, the values of  $|\overline{U}_1^{(1)}|$  change significantly as  $\alpha_{\text{ins}}$  varies from  $\alpha_{\text{ins}}(\omega_{\text{lb}}/2)$  to  $\alpha_{\text{ins}}(\omega_{\text{ub}})$ . In the range of smaller (i.e., the TS) wave numbers, a unit amplitude suction at the surface produces a streamwise velocity perturbation that increases with  $R_{\delta^*}$ , whereas at the larger (i.e., the Rayleigh) wave numbers, the maximum value of  $|\overline{U}_1^{(1)}|$  remains comparable to the amount of applied suction in the entire range of Reynolds numbers considered in this study. Because of the great difference between streamwise velocity perturbations in these two cases, the  $|\overline{U}_1^{(1)}|$  values at  $\omega = \omega_{\text{mg}}$  and  $\omega = \omega_{\text{ub}}$  would have been almost zero on the scale of figure 5(b); hence, they have been multiplied by a factor of 10 in this figure. Consistent with the above trend, lower amplitudes of pressure perturbation (not shown here) were observed in the cases of large wave numbers. Moreover, the pressure perturbation at the larger wave numbers begins to slowly decay immediately away from the surface. This is unlike the response in the range of smaller wave numbers, where the pressure perturbation is nearly constant inside the boundary layer and begins to attenuate only outside of this region.

Because of the large  $|\overline{U}_1^{(1)}|$  perturbations in the TS-wave-number range, the unsteady forcing function in equation (3.6a) would be expected to be dominated by the momentum transfer terms involving the perturbation in the streamwise velocity. Because the forcing term in equation (3.6a) accounts for the entire suction-induced receptivity, the values of the efficiency function  $\Lambda_u^{(1)}$  can be expected to be much greater for the range of viscous TS modes than for the range of inflectional instability modes. Although the transverse gradients associated with the Stokes wave become sharper in the frequency range of inflectional instabilities, they do not significantly alter the above conclusion as is shown later in section 4.3.

The mean flow perturbations produced by weak and nearly sinusoidal variations in the surface geometry will be examined next for the same set of values of  $\alpha_{\text{ins}}$ ,  $R_{\delta^*}$ , and  $\beta$  as previously chosen for figures 4 and 5. In figures 6 and 7, respectively, the  $|\overline{V}_1^{(3)}|$  and  $|\overline{U}_1^{(3)}|$  profiles are plotted after normalizing them by the local nondimensional amplitude of the surface height variation. Because  $|\overline{V}_1^{(3)}| = 0$  at the wall in

this case, the maximum of the vertical velocity perturbation occurs at a finite distance away from the surface. In the range of smaller (i.e., TS) wave numbers, this maximum occurs in the outer part of the boundary layer region; at larger wave numbers, the maximum shifts much closer to the wall and presumably lies just outside of the thin viscous layer next to the surface. Furthermore, at larger wave numbers, the  $|\overline{V}_1^{(3)}|$  profiles also exhibit a significant decay across the main part of the boundary layer.

The mean flow perturbations caused by the wall geometry variation are effectively driven by a shearing velocity at  $Y = 0$ , which arises from a transfer of boundary condition to the unperturbed location of the surface. (See eq. (3.5c).) Figures 6(b) and 7(b) show that the effect of this shear is quite significant in the entire boundary layer when the wave number is small. However, at larger wave numbers, this boundary perturbation is greatly attenuated across the viscous sublayer close to the wall. Although  $|\overline{U}_1^{(3)}|$  is many times greater than  $|\overline{V}_1^{(3)}|$  in this thin sublayer, both  $|\overline{U}_1^{(3)}|$  and  $|\overline{V}_1^{(3)}|$  have comparable magnitudes in the rest of the boundary layer. This also leads to a significant variation in the pressure perturbation  $\overline{P}_1^{(3)}$  across the boundary layer at these larger wave numbers.

Similar characteristics of mean flow perturbation caused by a wall geometry variation were noted at values of  $\beta$  other than  $-0.14$ . However, the overall magnitude of the mean flow perturbation was a decreasing function of the adverse pressure gradient  $|\beta|$  and eventually approached zero in the limit of the separation profile. Of course, the linear assumption is not valid in this limit, and mean flow separation is a possibility even for small perturbations in the surface height. Thus, the results for wall geometry-induced receptivity in the case of  $\beta = -0.1988$  should be regarded mainly as qualitative indicators of the limiting response expected under severely adverse pressure gradients.

### 4.3. Efficiency Functions for Localized Receptivity in Falkner-Skan Boundary Layers

The pressure gradient effect on the efficiency function for each of the receptivity mechanisms will be studied next. Recall that the admittance variation does not produce any mean flow perturbation but leads to a direct generation of instabilities through the short-scale, unsteady mass flux across the porous surface. (See refs. 32 and 33.) Thus, the effect of an adverse pressure gradient on this receptivity process will also be investigated.

The results presented in this section include the variation of the efficiency function  $\Lambda_u^{(j)}$  along three different paths in the  $\omega$ - $R_{\delta^*}$  plane. First, the change in  $|\Lambda_u^{(j)}|$  is examined as the acoustic frequency is varied while the wall inhomogeneity is held at a fixed location. In practice, the receptivity sites on an LFC wing are partially predetermined by the design process (e.g., at the joints between two adjacent parts, suction strips, and/or suction slots). Thus, to understand the frequency dependence of each receptivity mechanism and to determine the frequencies which are excited most efficiently at a given receptivity location would be useful. However, from the viewpoint of LFC design, the efficiency function for a disturbance of fixed (physical) frequency is of greatest interest because a typical design objective is to minimize the instability amplitudes in the most unstable band of frequencies. Thus, the variation in the magnitude of the efficiency functions is considered with respect to location for frequencies that are most relevant to the transition process. Finally, the variation in  $|\Lambda_u^{(j)}|$  along the two neutral branches is briefly examined. Such results can reveal useful information about the asymptotic scaling of the efficiency functions and may help to model the receptivity stage as part of more sophisticated transition prediction methods which depend on understanding the initial amplitudes of boundary layer disturbances. Moreover, results for receptivity caused by distributed surface nonuniformities can also be deduced quite easily from the efficiency function values for localized inhomogeneity along the lower branch of the neutral stability curve. (See refs. 36, 54, and 55.) The receptivity along the upper branch has little practical significance of its own but is of interest because it typifies the entire class of inflectional instabilities.

**4.3.1. Frequency dependence at fixed location of surface inhomogeneity.** First, consider the frequency dependence of the efficiency functions at a fixed location of the surface inhomogeneity. Figures 8 and 9 are plots of the values of  $|\Lambda_u^{(j)}|$  as functions of  $\omega$  for the wall suction ( $j = 1$ ) and wall admittance ( $j = 2$ ) problems, respectively. In each figure, data plots correspond to pressure gradients of  $\beta = -0.05, -0.10, -0.14,$  and  $-0.1988$ . (Note the different abscissa scales for different values of  $\beta$ .) Observe that the values of both  $|\Lambda_u^{(1)}|$  and  $|\Lambda_u^{(2)}|$  decrease monotonically (or very nearly so) as the frequency parameter is increased, which suggests that the generation of the high-frequency inflectional modes by these two mechanisms is inefficient in comparison with the generation of the low-frequency viscous TS

modes. However, decreased efficiency does not necessarily mean lower initial amplitudes in practice because the latter are also affected by the geometry of the suction strips (eq. (3.9b)). The rather narrow suction strips used for typical laminar flow control may favor the inviscid modes. Also note that both  $|\Lambda_u^{(1)}|$  and  $|\Lambda_u^{(2)}|$  decrease more rapidly with  $\omega$  across the rather small band of viscous TS (i.e., low-frequency) instabilities than across the much wider range of inflectional Rayleigh (i.e., relatively high-frequency) modes. A comparison of the efficiency function magnitudes for neutral frequencies at  $R_{\delta^*} = 1000$  for different values of  $\beta$  indicates that the efficiency function magnitude increases marginally with the adverse pressure gradient in the TS case and decreases somewhat in the inflectional-mode case. The increase in  $|\Lambda_u^{(j)}|$  ( $j = 1, 2$ ) with  $-\beta$  in the TS range is also consistent with the asymptotic predictions of Kerschen and Choudhari (ref. 32) and Choudhari. (See ref. 33.)

The triple-deck arguments in references 32 and 33 clearly show that the suction-induced receptivity in the TS range of frequencies is dominated by the transfer of streamwise momentum (i.e., the  $X$ -momentum equation) from the first-order perturbations  $\Psi_1^{(1)}$  and  $\psi_0$  to the short-scale unsteady field  $\psi_1^{(1)}$  containing the instability wave. The streamwise velocity perturbations are dominant in the range of TS modes because the streamwise wavelengths of these modes are much greater than the transverse boundary layer length scale (i.e., the displacement thickness  $\delta^*$ ). However, because the wavelengths of the inflectional modes are of the same order as  $\delta^*$ , the vertical momentum transfer was investigated for its importance during the generation of these instability modes. Evaluation of the separate contributions to  $|\Lambda_u^{(j)}|$  from the  $X$ - and  $Y$ -momentum equations showed that the role of vertical momentum transfer is again quite insignificant. This probably results because the energy transfer is localized in the thin viscous layers close to the wall where all velocity perturbations are primarily in the streamwise direction even in the range of predominantly inviscid instabilities.

Note that in the case of receptivity from wall suction or wall admittance variations previously discussed, there was no qualitative change in the efficiency function curves as the adverse pressure gradient was increased. However, when the receptivity is induced by wall geometry variations (fig. 10), the response of the efficiency function curve depends significantly on the value of  $\beta$ . As seen in figure 10(a)

for  $\beta = -0.05$ , the efficiency function  $|\Lambda_u^{(3)}|$  increases in magnitude almost up to the upper branch neutral frequency  $\omega_{\text{ub}}$  at both  $R_{\delta^*} = 500$  and  $R_{\delta^*} = 1000$ . However, with a further increase in  $R_{\delta^*}$ , the maximum value of the  $|\Lambda_u^{(3)}|$  curve quickly begins to shift toward lower frequencies and approaches the most unstable frequency  $\omega_{\text{mg}}$  at  $R_{\delta^*} = 1500$  and  $2000$ . Most likely, this is caused by a slow onset of inviscid mode dominance under a weak adverse pressure gradient. The  $|\Lambda_u^{(3)}|$  curve at  $\beta = -0.10$  displays a somewhat different response than that at  $\beta = -0.05$ . In this case, the maximum value of  $|\Lambda_u^{(3)}|$  at  $R_{\delta^*} = 500$  is already closer to  $\omega_{\text{mg}}$ ; however, at higher Reynolds numbers, this maximum is replaced by a peak at a much lower frequency. The  $|\Lambda_u^{(3)}|$  curve now displays a pronounced minimum between  $\omega = \omega_{\text{mg}}$  and  $\omega = \omega_{\text{ub}}$ . Figure 10(c) for  $\beta = -0.14$  also shows a roughly similar characteristic.

A comparison of figures 10(a)–10(c) also indicates that the overall maximum value of the  $|\Lambda_u^{(3)}|$  curve decreases, albeit rather weakly, with an increase of  $|\beta|$  and/or  $R_{\delta^*}$ . However, observe that a sudden increase in the efficiency function value occurs in the range of both low and high frequencies for the case of the separation profile (fig. 10(d)). The low-frequency (i.e.,  $\omega R_{\delta^*} \leq O(1)$ ) results are of doubtful accuracy because of the Stokes wave approximation for  $\psi_0$ . Nevertheless, the high-frequency results point toward an increase in the efficiency of wall geometry-induced receptivity under severely adverse pressure gradients. As noted before, remember that the maximum roughness height for which the mean flow perturbation can be regarded as a linear perturbation of the upstream flow decreases as the adverse pressure gradient increases. At  $\beta = -0.1988$ , even a minute roughness can provoke local separation and invalidate this analysis in principle. However, refer to the remarks at the end of this section in the same context.

Recall from the governing equations (3.6a) and (3.6b) that the wall geometry-induced receptivity equals the sum of two separate contributions: the first from the interaction of the Stokes wave with the mean flow perturbation, which leads to the volumetric source term in equation (3.6a) and the second from a direct scattering of the Stokes wave by the geometric inhomogeneity, which leads to the inhomogeneous boundary condition for equation (3.6b). Both of these contributions have the same order of magnitude in the Blasius case (refs. 36 and 37); whereas the mean flow perturbation is zero to the leading order in the separation profile case, and hence, the receptivity there results entirely from the inhomogeneous bound-

ary condition. A comparison of these two contributions at intermediate values of the pressure gradient parameter (fig. 11) reveals that, for frequencies closer to  $\omega_{\text{lb}}$  where the instability is primarily viscous, the contribution because of the mean flow perturbation is small but still significant. However, at higher frequencies which lead to shorter wavelength inflectional instabilities, this contribution becomes quite negligible relative to the contribution from equation (3.6b). This characteristic is completely consistent with the theoretical prediction of Goldstein (ref. 21) that the cause is the short-wavelength nature of the inflectional instabilities, which dominate the range of higher frequencies. As discussed in the context of figures 6 and 7, the mean flow perturbation decreases in amplitude as the length scale of the surface disturbance decreases, whereas the thickness of the Stokes shear wave decreases as the frequency increases, which makes the same wall roughness element appear taller in a relative sense.

Finally, note that because the mean flow perturbation produced by a wall geometry variation becomes small as  $\beta \rightarrow -0.1988$ , the receptivity in the above limit is dominated by the direct scattering of the Stokes wave. Therefore, it is quite possible that the efficiency function results presented in this paper would remain quantitatively satisfactory even at  $\beta = -0.1988$ .

**4.3.2. Reynolds number dependence for fixed-frequency disturbances.** The efficiency functions that correspond to an acoustic disturbance of a fixed physical frequency are now considered. Figure 12 indicates the variation in the magnitude of the efficiency function  $\Lambda_u^{(1)}$  with respect to the wall inhomogeneity location  $R_{\delta^*}$  for adverse pressure gradients that correspond to  $\beta = -0.05$ ,  $-0.10$ ,  $-0.14$ , and  $-0.1988$ . In descending order, the four frequencies selected for each value of  $\beta$  correspond to those with amplification ratios of  $e^5$ ,  $e^7$ ,  $e^9$ , and  $e^{11}$  between the two neutral locations. Thus, on the basis of the  $e^9$  criterion, the third highest frequency at each  $\beta$  is the one most likely to lead to transition. The lower branch, the upper branch, and the maximum-growth locations at each frequency are indicated on each curve in figures 12–14 by a triangle, a circle, and a diamond, respectively. Note that because of the slow deceleration of the free stream, a disturbance of fixed physical frequency does not correspond to a constant dimensionless frequency parameter  $f = \omega^* \nu^* / U_e^{*2}$  as in the Blasius case but  $f$  varies as  $f_{\text{lb}} (R_{\delta^* \text{lb}} / R_{\delta^*})^{2\beta}$  as  $R_{\delta^*}$  varies. The values of  $f_{1000}$  indicated in figures 12–14 correspond to the

frequency parameter  $f$  based on a reference Reynolds number of  $R_{\delta^*} = 1000$ .

Two observations follow from figure 12. First, as the adverse pressure gradient increases, the range of amplified frequencies generally shifts toward higher values. Consequently, the maximum value of the  $|\Lambda_u^{(1)}|$  curve corresponding to an instability wave with a fixed amplification ratio decreases with an increase in the adverse pressure gradient. At  $\beta = -0.14$ , the maximum value of  $|\Lambda_u^{(1)}|$  is approximately 55 percent less than the maximum value at a frequency that has the same amplification ratio in the zero pressure gradient case studied in references 36 and 37. Secondly, the relative decrease in  $|\Lambda_u^{(1)}|$  between the maximum growth rate location and the upper branch location is rather insignificant when the pressure gradient is weak but becomes quite large as the pressure gradient increases. As shown in figure 12(c), the efficiency function at  $\beta = -0.14$  decreases in value at nearly a constant rate as the wall inhomogeneity moves from the lower to near the upper branch location.

As in the previous wall suction case, figure 13 shows that the efficiency function  $|\Lambda_u^{(2)}|$  for the wall admittance-induced receptivity also decreases in value with an increase in the adverse pressure gradient. Unlike  $|\Lambda_u^{(1)}|$ , the overall shape of the  $|\Lambda_u^{(2)}|$  curve is relatively unaffected by the precise value of the pressure gradient parameter  $\beta$ .

The efficiency function  $\Lambda_u^{(3)}$  for the receptivity caused by a wall geometry variation is plotted in figure 14 for the same frequencies as those in figures 12 and 13. Note that the maximum value of the  $|\Lambda_u^{(3)}|$  curve for an instability wave with a specified amplification ratio undergoes only a slight change as  $|\beta|$  is increased from 0.05 to 0.10 in spite of the shift in the instability band toward higher frequencies. Moreover, for wall hump locations upstream of the lower branch, the efficiency function curve is almost a linear function of  $R_{\delta^*}$  at all values of  $|\beta|$ . However, the nature of receptivity downstream of the lower branch location appears to be highly dependent on the magnitude of the applied pressure gradient. Figure 14 also shows that, with increasing  $|\beta|$ , the overall maximum of the  $|\Lambda_u^{(3)}|$  curve shifts from the upper branch toward the lower branch location. Furthermore, in the limiting case of  $\beta = -0.1988$  (fig. 14(d)), the maximum magnitude of the efficiency function at each of the chosen frequencies is significantly greater than at any other value of  $\beta$ .

#### 4.3.3. Variation along two neutral branches and implications for distributed receptivity.

Figure 15 displays the variation in the magnitude of the efficiency functions  $|\Lambda_u^{(j)}|$  ( $j = 1, 2, 3$ ) along the lower branch of the neutral stability curve. The first observation from figure 15 is that the slope of each efficiency function curve in the separation case is quite different from that of a relatively moderate adverse pressure gradient. This is only natural because of the different scaling laws for the instability wave frequency and wave number along the lower branch of the neutral stability curve at  $\beta = -0.1988$ . (See section 4.1.) Of course, as discussed in section 4.3, the results for  $|\Lambda_u^{(1)}|$  and  $|\Lambda_u^{(3)}|$  at  $\beta = -0.1988$  are to be regarded with caution because the Stokes wave approximation was utilized to calculate these quantities. The  $|\Lambda_u^{(2)}|$  curves (fig. 15(b)), which are independent of the Stokes wave approximation, indicate that the efficiency function in the wall admittance case increases more rapidly with  $R_{\delta^*}$  at  $\beta = -0.1988$  than at other values of the pressure gradient parameter.

Also note in figure 15 that efficiency function curves at  $\beta = -0.05, -0.10$ , and  $-0.14$  are nearly parallel for each of the three types of surface inhomogeneities;  $|\Lambda_u^{(1)}|$  and  $|\Lambda_u^{(2)}|$  increase as a function of  $|\beta|$ , whereas  $|\Lambda_u^{(3)}|$  decreases somewhat with an increase in the adverse pressure gradient. The high-Reynolds-number asymptotes in the first two cases (i.e.,  $|\Lambda_u^{(1)}| = O(R_{\delta^*}^{1/2})$  and  $|\Lambda_u^{(2)}| = O(R_{\delta^*}^{1/4})$ ) are also established at fairly low Reynolds numbers, somewhere in the range of  $R_{\delta^*} = 1000$  to  $R_{\delta^*} = 2000$ , depending on the precise value of the adverse pressure gradient parameter. In contrast, figure 15(c) indicates that the efficiency function  $|\Lambda_u^{(3)}|$  in the wall roughness case does not quite reach its asymptote,  $|\Lambda_u^{(3)}| = O(R_{\delta^*}^0)$ , even for Reynolds numbers as high as 50 000, especially under severely adverse pressure gradients. However, for  $R_{\delta^*} \geq 5000$ , the difference between the analytical (i.e., triple-deck) and the numerical predictions (refs. 21, 32, and 33) for all three efficiency functions was generally less than 10 percent.

Previously (refs. 54 and 55), the receptivity caused by distributed (i.e., nonlocalized) surface nonuniformities was shown to be dominated by a narrow range of locations near the lower branch of the neutral stability curve. In the present context, this implies that the receptivity in such cases is determined by the TS-mode generation and that the generation of Rayleigh modes is primarily relevant

to isolated nonuniformities with a shorter streamwise length scale. The increase in receptivity caused by nonlocalized distributions of surface nonuniformities is quantified by the equation

$$\frac{C_{u,\text{array}}^{(j)}}{C_u^{(j)}} = \frac{\alpha_{\text{ins,lb}}}{\bar{F}^{(j)}(\alpha_{\text{ins,lb}}) \sqrt{i\pi\tilde{D}_\alpha}} \sum_{n=1}^{\infty} \bar{F}^{(j)}(n\alpha_{w,\text{lb}}) \times \exp\left[-\frac{(n\alpha_{w,\text{lb}} - \alpha_{\text{ins,lb}})^2}{i\tilde{D}_\alpha}\right] \quad (4.1a)$$

(refs. 56 and 57), which yields the ratio of the effective coupling coefficient (refs. 58 and 59) for an array of compact equidistant nonuniformities to the coupling coefficient in the case of a single such nonuniformity whose shape is given by  $F^{(j)}(X)$ . Here,  $\alpha_w(R_{\delta^*}) \equiv \alpha_w^* \delta^*(R_{\delta^*})$  denotes the fundamental wave number of the periodic distribution; the quantity  $\tilde{D}_\alpha$  is defined as

$$\tilde{D}_\alpha = \left(\frac{R_{\delta^*,\text{lb}}^2}{R_{\ell^*,\text{lb}}}\right) D_\alpha \quad (4.1b)$$

where the desynchronization factor  $D_\alpha$  is given by

$$D_\alpha = \frac{2}{2 - \beta} (\alpha'_{\text{ins,lb}} - \alpha'_{w,\text{lb}}) \quad (4.1c)$$

in the present notation. The primes in equation (4.1c) denote differentiation with respect to  $R_{\delta^*}$ , and the subscript lb indicates evaluation at the lower branch location  $R_{\delta^*} = R_{\delta^*,\text{lb}}$ . The desynchronization factor is a measure of how rapidly the unsteady forcing produced by the interaction between the free-stream and surface disturbances becomes detuned with respect to the phase of the instability mode. In figure 16, the values of  $|D_\alpha|$  are plotted for the values of  $\beta$  that are being considered in this parametric study. For comparison, the  $|D_\alpha|$  curve for the Blasius boundary layer has also been included in this plot. The figure shows that, except in the case of the separation profile, the value of  $|D_\alpha|$  is relatively insensitive to the value of  $\beta$ . This implies that the asymptotic scalings as well as other observations made for the Blasius boundary layer ( $\beta = 0$ ) in references 54, 55, 58, and 59 are also valid in the context of distributed receptivity in moderately adverse pressure gradient boundary layers.

Now, the efficiency functions for the inflectional (i.e., Rayleigh) modes will be studied from the perspective of their variation along the upper branch of the neutral stability curve. (See fig. 17.) Observe that, despite the Reynolds number dependence

of both the mean flow perturbation and the Stokes shear wave, the efficiency functions  $|\Lambda_u^{(1)}|$  and  $|\Lambda_u^{(3)}|$  are asymptotic to a constant at sufficiently high Reynolds numbers just as was the efficiency function  $|\Lambda_u^{(2)}|$  in the wall admittance case which does not depend on either the mean-flow disturbance or the Stokes shear wave. The order in which the high- $R_{\delta^*}$  asymptote is reached at any given pressure gradient corresponds to  $|\Lambda_u^{(2)}|$ ,  $|\Lambda_u^{(1)}|$ , and  $|\Lambda_u^{(3)}|$ . The same trend was also observed along the lower branch; hence, the finite Reynolds number effect appears overall to be the most significant in the case of receptivity caused by the wall geometry variations. However, for each type of surface inhomogeneity, the finite Reynolds number effect diminishes uniformly with an increasingly adverse pressure gradient. Thus, the constant asymptotes for all three efficiency functions are approximately valid for  $R_{\delta^*} > 5000$  at  $\beta = -0.05$ , for  $R_{\delta^*} > 2500$  at  $\beta = -0.10$ , and  $R_{\delta^*} > 1000$  at  $\beta = -0.14$ . In the case of the separation profile, the efficiency functions are almost constant throughout the range of Reynolds numbers investigated.

## 5. Summary and Concluding Remarks

A finite Reynolds number approach was used to examine the influence of an adverse pressure gradient on the efficiency of acoustic receptivity through localized surface disturbances that involve short-scale variations in the wall suction velocity, wall admittance, or the shape of the airfoil surface. The stability of boundary layer flows that develop under adverse pressure gradients is governed by the viscous TS mechanism at lower values of the frequency parameter and/or Reynolds number (i.e., near the lower branch of the neutral stability curve), whereas the inviscid inflectional mechanism is dominant in the remainder of the unstable region. Although receptivity in the lower branch region is usually more important from a practical point of view, the possibility of highly efficient excitation of the inflectional instabilities cannot be ignored *a priori*. For problems of this type, the finite Reynolds number extension of the Goldstein-Ruban theory provides a particularly useful predictive tool because of its inherent composite nature (i.e., valid for a combination of instability regimes) and its flexible adaptation to the different types of surface inhomogeneities. In addition, this particular extension of the theory can possibly capture some higher order terms in the asymptotic expansion based on  $R_{\delta^*} \gg 1$ . However, in practice, the overall accuracy of such a prediction may not be significantly better than a leading order asymptotic solution because the overall error may

be dominated by the neglected  $O\left\{\left[\epsilon_w^{(j)}\right]^2 \epsilon_{fs}\right\}$  term in both cases. The Falkner-Skan family of self-similar boundary layer profiles was chosen herein to systematically investigate the effects of an adverse pressure gradient parameter. However, the overall trends encountered here are also expected to remain valid for the nonsimilar boundary layers that are encountered in practice.

The overall conclusion from the parametric study is that the adverse pressure gradient reduces the maximum value of the efficiency function that is related to the receptivity caused by wall suction or wall admittance variation, but it does not significantly affect the magnitude of the efficiency function related to wall geometry-induced receptivity (except for the increase seen under severely adverse pressure gradients). These trends appear to have their origin in the high-frequency and short-wavelength nature of the instabilities that are most critical for the transition in adverse pressure gradient boundary layers. In the wall suction case, the shorter wavelengths cause the corresponding mean flow perturbations to become smaller in magnitude, thereby weakening the interaction with the Stokes shear wave that produces the instabilities. Similarly, the efficiency of admittance-induced receptivity decreases because the shortened streamwise length scales and commensurately increased unsteady vertical perturbation components inside the boundary layer make any given magnitude of the unsteady normal flux at the wall relatively less effective in producing the instability wave. For the case of wall geometry-induced receptivity, the mean flow perturbation caused by a specified wall height variation becomes weaker at larger wave numbers, but the maximum value of the efficiency function  $|\Lambda_u^{(j)}|$  remains relatively constant as  $|\beta|$  is increased and, in fact,  $|\Lambda_u^{(j)}|$  increases somewhat as  $|\beta|$  becomes very large. This is because the wall geometry-induced receptivity has a second component that is related to a purely geometric interaction of the Stokes shear wave with the local distortion in the surface. This latter interaction is influenced by two opposing effects; the reduced thickness of the Stokes shear wave at high frequencies makes a surface perturbation of fixed height appear relatively greater and a weakened transmission of the horizontal velocity perturbation (which arises from the transfer of the no-slip boundary condition) to the boundary layer region controlling the instability. The numerical results indicate that these two effects almost cancel each other and thereby keep the maximum value of  $|\Lambda_u^{(3)}|$  almost constant for much of the  $\beta$  range.

The previous conclusions concerning the differences between the efficiency factors for viscous and inviscid types of instabilities should not be extrapolated directly to the actual amplitudes of these instabilities in any given situation. Even when the localized mechanisms considered here dominate the overall receptivity process, the amplitudes of the generated instability modes are determined not only by the efficiency factor but also by the geometry of the surface disturbance and the frequency spectrum of the free-stream disturbances. Because the ranges of wavelengths and frequencies for these two instabilities are quite different even at finite Reynolds numbers, a specific wall inhomogeneity will not necessarily have a spatial spectrum that is nearly uniform across the entire range of wave numbers. Similarly, the disturbance environment is unlikely to have a relatively flat spectrum in the range of frequencies corresponding to both types of instabilities. Hence, more precise conclusions for initial amplitudes of the two types of instability waves will necessarily depend upon more specific information.

NASA Langley Research Center  
Hampton, VA 23681-0001  
November 15, 1994

## References

1. Schubauer, G. B.; and Skramstad, H. K.: *Laminar-Boundary-Layer Oscillations and Transition on a Flat Plate*. NACA Rep. 909, 1948.
2. Holmes, Bruce J.: NLF Technology Is Ready To Go. *Aerosp. America*, vol. 26, Jan. 1988, pp. 16, 19, and 20.
3. Bushnell, D. M.; and Malik, M. R.: Application of Stability Theory to Laminar Flow Control—Progress and Requirements. *Stability of Time Dependent and Spatially Varying Flows*, D. L. Dwoyer and M. Y. Hussaini, eds., Springer-Verlag, 1987, pp. 1–17.
4. Herbert, T.; and Bertolotti, F. P.: Effect of Pressure Gradients on the Growth of Subharmonic Disturbances in Boundary Layers. *Proceedings of the Conference on Low Reynolds Number Airfoil Aerodynamics*, T. J. Mueller, ed., Univ. Notre Dame, 1985, pp. 65–76.
5. Goldstein, M. E.; and Hultgren, Lennart S.: A Note on the Generation of Tollmien-Schlichting Waves by Sudden Surface-Curvature Change. *J. Fluid Mech.*, vol. 181, Aug. 1987, pp. 519–525.
6. Schlichting, H.; and Ulrich, A.: Zur Berechnung der Umschlages Laminar/Turbulent. *Jahrb. 1942 der deutschen Luftfahrtforschung*, R. Oldenbourg (Munich), pp. I 8–I 35.
7. Pretsch, J.: Die Stabilität Einer Ebener Laminarströmung bei Druckgefälle und Druckanstieg. *Jahrb.*

- 1941 der deutschen Luftfahrtforschung, R. Oldenbourg (Munich), pp. I 158–I 175.
8. Wazzan, A. R.; Okamura, T. T.; and Smith, A. M. O.: *Spatial and Temporal Stability Charts for the Falkner-Skan Boundary-Layer Profiles*. DAC-67086, McDonnell-Douglas Astronaut. Co., 1968. (Available from DTIC as AD 712 198.)
  9. Saric, William S.; and Nayfeh, Ali Hasan: Nonparallel Stability of Boundary Layers With Pressure Gradients and Suction. *Laminar-Turbulent Transition*, AGARD-CP-224, Oct. 1977, pp. 6-1–6-21.
  10. Mack, Leslie M.: Transition Prediction and Linear Stability Theory. *Laminar-Turbulent Transition*, AGARD-CP-224, Oct. 1977, pp. 1-1–1-22.
  11. Kloker, M.; and Fasel, H.: Numerical Simulation of Two- and Three-Dimensional Instability Waves in Two-Dimensional Boundary Layers With Streamwise Pressure Gradient. *Laminar-Turbulent Transition*, D. Arnal and R. Michel, eds., Springer-Verlag, 1990, pp. 681–686.
  12. Wubben, F. J. M.; Passchier, D. M.; and Van Ingen, J. L.: Experimental Investigation of Tollmien-Schlichting Instability and Transition in Similar Boundary Layer Flow in an Adverse Pressure Gradient. *Laminar-Turbulent Transition*, D. Arnal and R. Michel, eds., Springer-Verlag, 1990, pp. 31–42.
  13. Watmuff, J. H.: Turbulent Spots in an Adverse Pressure Gradient. *Bull. American Phys. Soc.*, vol. 35, no. 10, Nov. 1990, pp. 2261–2263.
  14. Leehey, P.; and Shapiro, P.: Leading Edge Effect in Laminar Boundary Layer Excitation by Sound. *Laminar-Turbulent Transition*, R. Eppler and H. Fasel, eds., Springer-Verlag, 1980, pp. 321–331.
  15. Obremski, H. J.; Morkovin, M. V.; and Landahl, M.: *A Portfolio of Stability Characteristics of Incompressible Boundary Layers*. AGARDograph 134, Mar. 1969.
  16. Morkovin, Mark V.: *Critical Evaluation of Transition From Laminar to Turbulent Shear Layers With Emphasis on Hypersonically Traveling Bodies*. AFFDL-TR-68-149, U.S. Air Force, Mar. 1969. (Available from DTIC as AD 686 178.)
  17. Kachanov, I. U. S.; Kozlov, V. V.; and Levchenko, V. I. A.: Occurrence of Tollmien-Schlichting Waves in the Boundary Layer Under the Effect of External Perturbations. *Fluid Dyn.*, vol. 13, no. 5, Mar. 1979, pp. 704–711.
  18. Aizin, L. B.; and Polyakov, M. F.: Acoustic Generation of Tollmien-Schlichting Waves Over Local Unevenness of Surface Immersed in Stream, Preprint 17, Akad. Nauk USSR, 1979.
  19. Murdock, J. W.: The Generation of a Tollmien-Schlichting Wave by a Sound Wave. *Laminar-Turbulent Transition*, R. Eppler and H. Fasel, eds., Springer-Verlag, 1980, pp. 332–340.
  20. Goldstein, M. E.; Sockol, P. M.; and Sanz, J.: The Evolution of Tollmien-Schlichting Waves Near a Leading Edge. *J. Fluid Mech.*, vol. 127, Feb. 1983, pp. 59–81.
  21. Goldstein, M. E.: Scattering of Acoustic Waves Into Tollmien-Schlichting Waves by Small Streamwise Variations in Surface Geometry. *J. Fluid Mech.*, vol. 154, May 1985, pp. 509–529.
  22. Goldstein, M. E.; Leib, S. J.; and Cowley, S. J.: Generation of Tollmien-Schlichting Waves on Interactive Marginally Separated Flows. *J. Fluid Mech.*, vol. 181, Aug. 1987, pp. 485–517.
  23. Reshotko, Eli: Boundary-Layer Stability and Transition. *Annual Review of Fluid Mechanics*, Volume 8, Milton van Dyke, Walter G. Vincenti, and J. V. Wehausen, eds., Annual Reviews, Inc., 1976, pp. 311–349.
  24. Ruban, A. I.: On the Generation of Tollmien Waves by Sound. *Fluid Dyn.*, vol. 19, no. 5, Sept.–Oct. 1984, pp. 709–716.
  25. Zavolskii, N. A.; Reutov, V. P.; and Rybushkina, G. V.: Vozbuzhdenie voln Tollmina-Shilkhtinga pri rasseianii akusticheskikh i vikhrevykh vozmushchenii v pogranchnom sloe na volnistoi poverkhnosti i. *PMTF—Zhurnal Prikladnoi Mekhaniki i Tekhnicheskoi Fiziki*, May–June 1983, pp. 79–86.
  26. Nishioka, M.; and Morkovin, M. V.: Boundary-Layer Receptivity to Unsteady Pressure Gradients—Experiments and Overview. *J. Fluid Mech.*, vol. 171, Oct. 1986, pp. 219–261.
  27. Goldstein, M. E.; and Hultgren, Lennart S.: Boundary-Layer Receptivity to Long-Wave Free-Stream Disturbances. *Annual Review of Fluid Mechanics*, vol. 21, John L. Lumley, Milton van Dyke, and Helen L. Reed, eds., Annual Reviews, Inc., 1989, pp. 137–166.
  28. Kerschen, Edward J.: Boundary Layer Receptivity. AIAA-89-1109, Apr. 1989.
  29. Chen, C. F., ed.: *Mechanics USA 1990—Proceedings of the Eleventh U.S. National Congress of Applied Mechanics*, ASME Press, 1990.
  30. Crouch, J. D.: Initiation of Boundary-Layer Disturbances by Nonlinear Mode Interactions. *Boundary Layer Stability and Transition to Turbulence*, D. C. Reda, H. L. Reed, and R. Kobayashi, eds., ASME, 1991, pp. 63–68.
  31. Bodonyi, R. J.; Tadjfar, M.; Welch, W. J. C.; and Duck, P. W.: A Numerical Study of the Interaction Between Unsteady Free-Stream Disturbances and Localized Variations in Surface Geometry. *J. Fluid Mech.*, vol. 209, Dec. 1989, pp. 285–308.
  32. Kerschen, E. J.; and Choudhari, M. M.: Boundary Layer Receptivity at a Suction Surface-Hard Wall Junction. *Bull. American Phys. Soc.*, vol. 30, no. 10, Nov. 1985, p. 1709.
  33. Choudhari, Meelan: Boundary Layer Receptivity Mechanisms Relevant to Laminar Flow Control. Ph.D. Diss., Univ. of Arizona, 1990.

34. Choudhari, M.; and Streett, C. L.: Interaction of a High-Speed Boundary Layer With Unsteady Free-Stream Disturbances. *Transitional and Turbulent Compressible Flows*, L. D. Kral, T. A. Zang, et al., eds., FED-Vol. 151, ASME, 1993, pp. 15–28.
35. Choudhari, Meelan; and Streett, Craig L.: Boundary Layer Receptivity Phenomena in Three-Dimensional and High-Speed Boundary Layers. AIAA-90-5258, Oct. 1990.
36. Choudhari, Meelan; and Streett, C. L.: *A Finite Reynolds Number Approach for the Prediction of Boundary Layer Receptivity in Localized Regions*. NASA TM-102781, 1991.
37. Choudhari, M.; and Streett, C. L.: A Finite Reynolds Number Approach for the Prediction of Boundary Layer Receptivity in Localized Regions. *Phys. Fluids A*, vol. 4, 1992, pp. 2495–2515.
38. Crouch, J. D.: Initiation of Boundary-Layer Disturbances by Nonlinear Mode Interactions. *Boundary Layer Stability and Transition to Turbulence*, D. C. Reda, H. L. Reed, and R. Kobayashi, eds., ASME, 1991, pp. 63–68.
39. Crouch, J. D.: Initiation of Boundary-Layer Disturbances by Nonlinear Mode Interactions. *Phys. Fluids A*, vol. 4, 1992, pp. 1408–1414.
40. Pal, A.; Bower, W. W.; and Meyer, G. H.: A Parametric Study of Boundary Layer Receptivity for an Acoustic Wave/Porous Plate Interaction. *Boundary Layer Stability and Transition to Turbulence*, D. C. Reda, H. L. Reed, and R. Kobayashi, eds., ASME, 1991, pp. 77–82.
41. Fedorov, A. V.: Excitation and Development of Unstable Disturbances in Unstable Boundary Layers. Ph.D. Diss., Moscow Institute of Physics and Technology, 1982.
42. Tumin, A. M.; and Fedorov, A. V.: Vozbuzhdenie voln neustoiichivosti v pogranichnom sloe na vibriruiushchei poverkhnosti. *PMTF—Zhurnal Prikladnoi Mekhaniki i Tekhnicheskoi Fiziki*, May–June 1983, pp. 72–79.
43. Choudhari, Meelan; Ng, Lian; and Streett, Craig L.: A General Approach for the Prediction of Localized Instability Generation in Boundary Layer Flows. *Boundary Layer Transition and Control*, R. Aeronaut. Soc., 1991, pp. 45.1–45.20.
44. Jiang, Feng; and Gaster, M.: A Fast Numerical Scheme for  $e^N$  Calculations. *Bull. American Phys. Soc.*, vol. 36, no. 10, 1991, p. 2712.
45. Saric, William S.; Hoos, Jon A.; and Radeztsky, Ronald H.: Boundary-Layer Receptivity of Sound With Roughness. *Boundary Layer Stability and Transition to Turbulence*, D. C. Reda, H. L. Reed, and R. Kobayashi, eds., ASME, 1991, pp. 17–22.
46. Ackerberg, R. C.; and Phillips, J. H.: The Unsteady Laminar Boundary Layer on a Semi-Infinite Flat Plate Due to Small Fluctuations in the Magnitude of the Free-Stream Velocity. *J. Fluid Mech.*, vol. 51, pt. 1, Jan. 1972, pp. 137–157.
47. Goldstein, M. E.; Sockol, P. M.; and Sanz, J.: The Evolution of Tollmien-Schlichting Waves Near a Leading Edge. II—Numerical Determination of Amplitudes. *J. Fluid Mech.*, vol. 129, Apr. 1983, pp. 443–453.
48. Smith, F. T.; Brighton, P. W. M.; Jackson, P. S.; and Hunt, J. C.: On Boundary-Layer Flow Past Two-Dimensional Obstacles. *J. Fluid Mech.*, vol. 113, Dec. 1981, pp. 123–152.
49. Smith, F. T.: On the Non-Parallel Flow Stability of the Blasius Boundary Layer. *Proc. R. Soc.*, vol. 366, no. 1724, May 1979, pp. 91–109.
50. Bodonyi, R. J.; and Smith, F. T.: The Upper Branch Stability of the Blasius Boundary Layer, Including Non-Parallel Flow Effects. *Proc. R. Soc.*, vol. 375, no. 1760, Feb. 1981, pp. 65–92.
51. Tam, C. K. W.: The Excitation of Tollmien-Schlichting Waves in Low Subsonic Boundary Layers by Free-Stream Sound Waves. *J. Fluid Mech.*, vol. 109, Aug. 1981, pp. 483–501.
52. Okamura, T. T.; Smith, A. M. O.; and Wazzan, A. R.: Stability of Laminar Boundary Layers at Separation. *Phys. Fluids*, vol. 10, 1967, pp. 2540–2545.
53. Hughes, T. H.; and Reid, W. H.: The Stability of Laminar Boundary Layers at Separation. *J. Fluid Mech.*, vol. 23, Dec. 1965, pp. 737–747.
54. Choudhari, Meelan: Boundary-Layer Receptivity Due to Distributed Surface Imperfections of a Deterministic or Random Nature. *Theoret. & Comput. Fluid Dyn.*, vol. 4, no. 3, Feb. 1993, pp. 101–118.
55. Choudhari, Meelan: *Boundary-Layer Receptivity Due to Distributed Surface Imperfections of a Deterministic or Random Nature*. NASA CR-4439, 1992.
56. Choudhari, Meelan: Roughness-Induced Generation of Crossflow Vortices in Three-Dimensional Boundary Layers. *Theoret. & Comput. Fluid Dyn.*, vol. 6, Feb. 1994, pp. 1–31.
57. Choudhari, Meelan: *Roughness-Induced Generation of Crossflow Vortices in Three-Dimensional Boundary Layers*. NASA CR-4505, 1993.
58. Choudhari, Meelan: *Distributed Acoustic Receptivity in Laminar Flow Control Configurations*. NASA CR-4438, 1992.
59. Choudhari, Meelan: Distributed Acoustic Receptivity in Laminar Flow Control Configurations. *Phys. Fluids A*, vol. 6, no. 2, Feb. 1994, pp. 489–506.

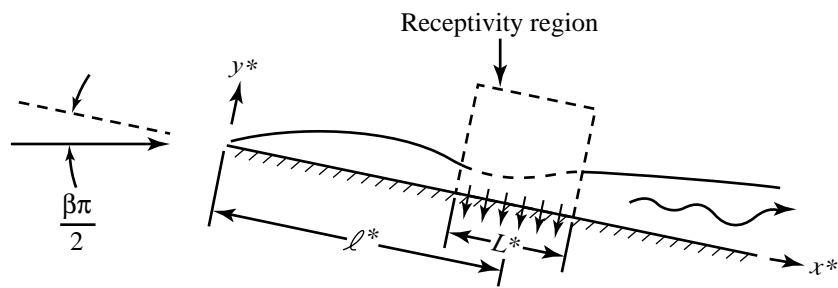
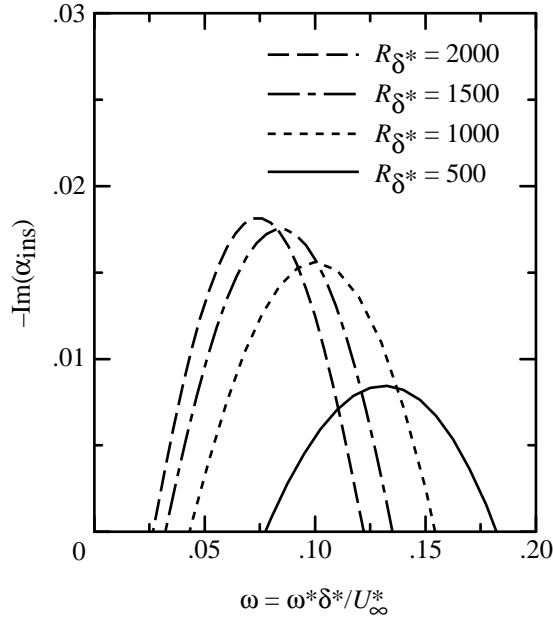
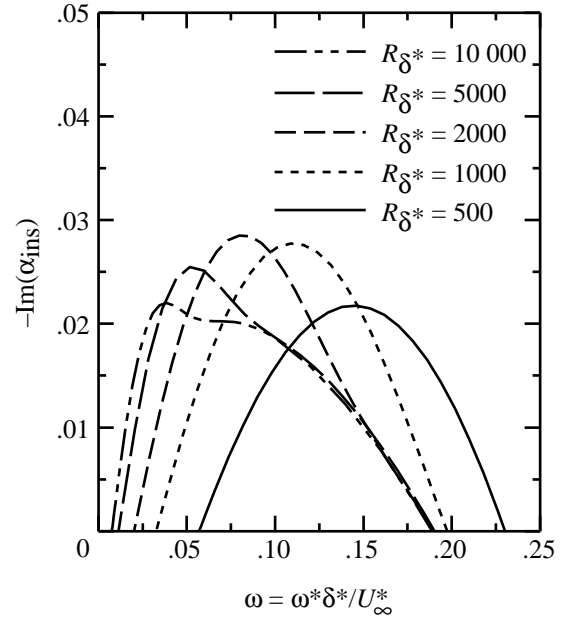


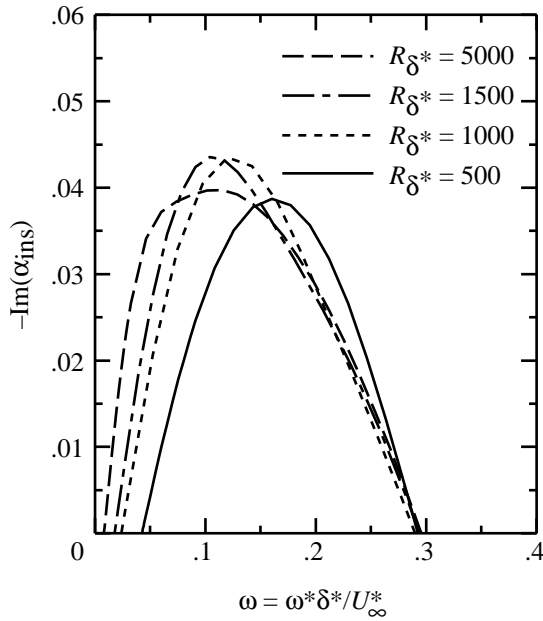
Figure 1. Sketch of the problem.



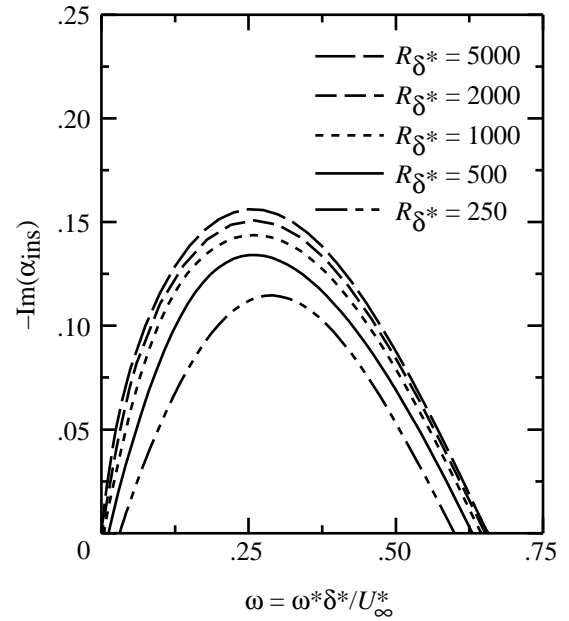
(a)  $\beta = -0.05$ .



(b)  $\beta = -0.10$ .



(c)  $\beta = -0.14$ .



(d)  $\beta = -0.1988$ .

Figure 2. Influence of adverse pressure gradient on streamwise growth rate of instability wave in Falkner-Skan profiles.

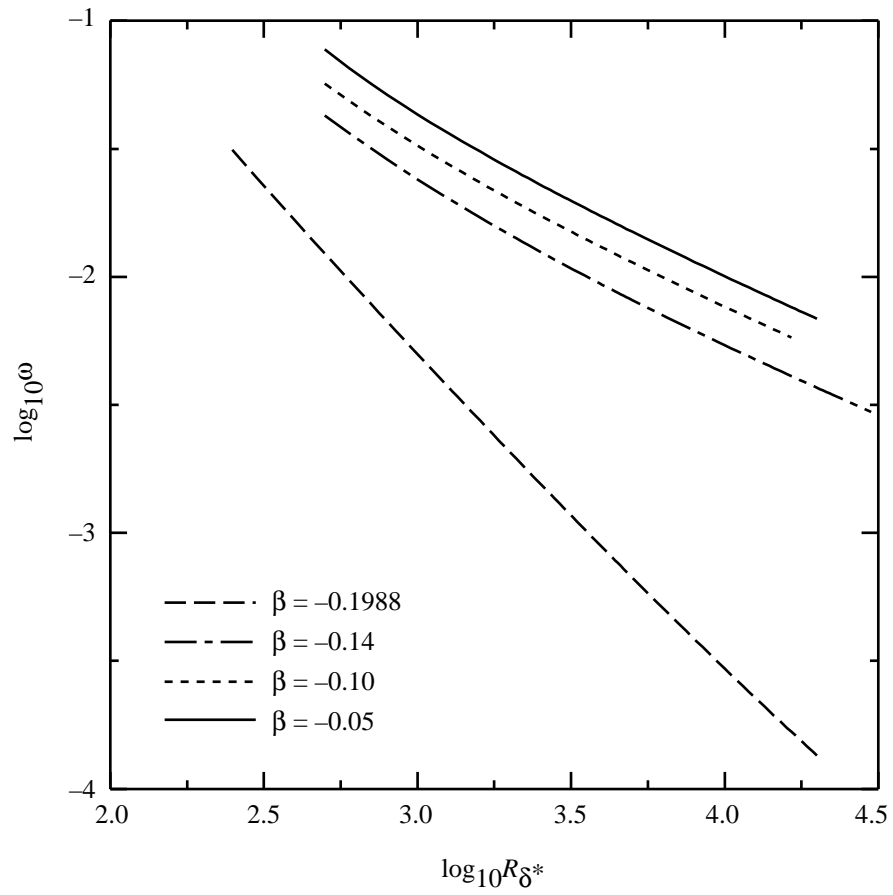
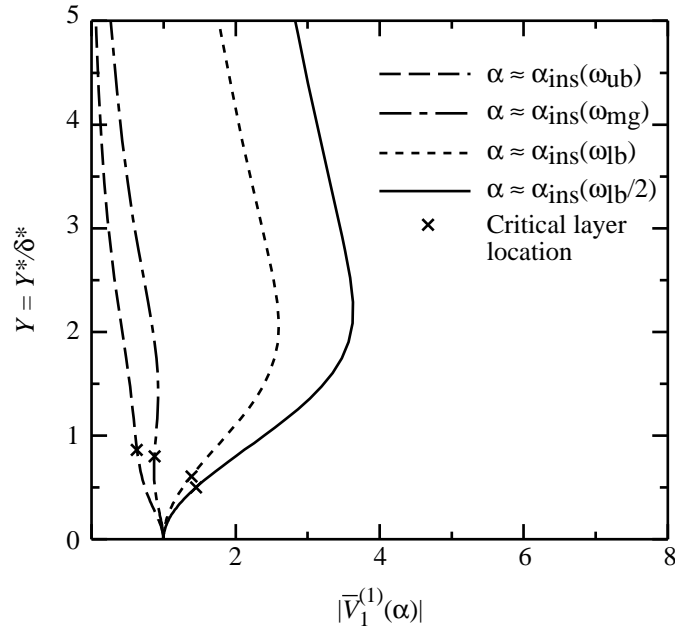
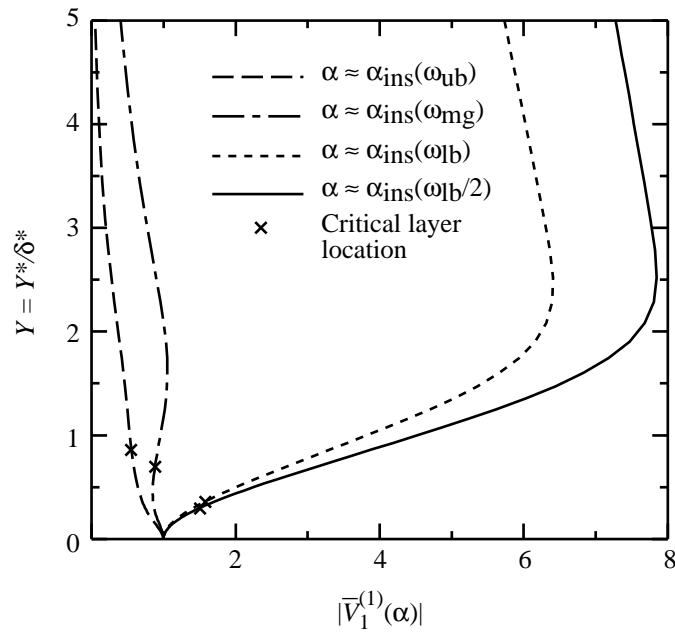


Figure 3. Nondimensional local frequency  $\omega$  along lower branch of neutral stability curve.

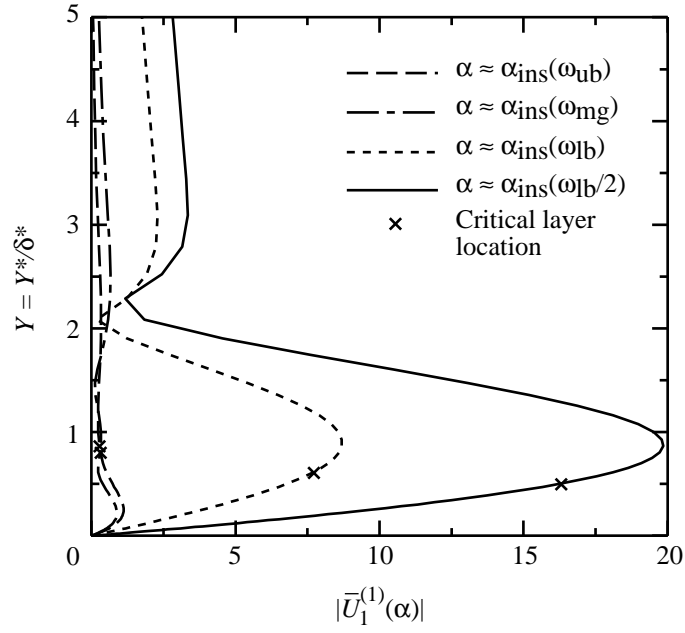


(a)  $\beta = -0.14$ ;  $R_{\delta^*} = 500$ .

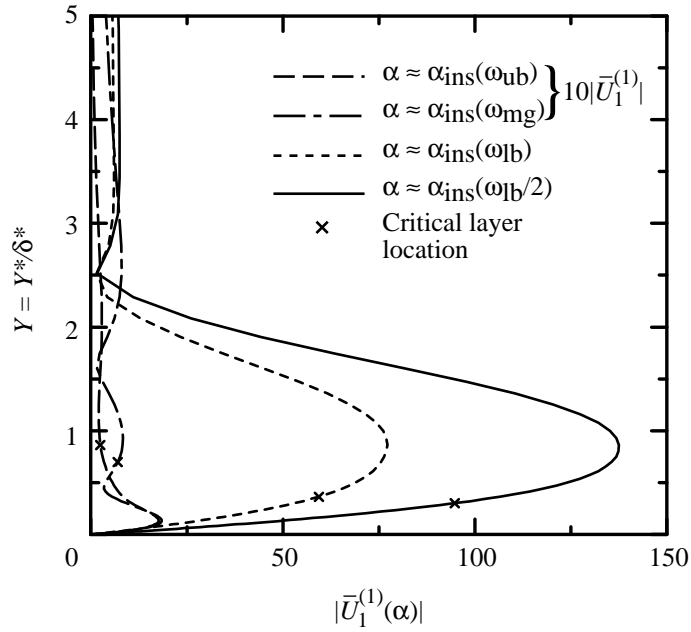


(b)  $\beta = -0.14$ ;  $R_{\delta^*} = 5000$ .

Figure 4. Mean vertical velocity perturbation produced by wave number  $\alpha$  of wall suction distribution.

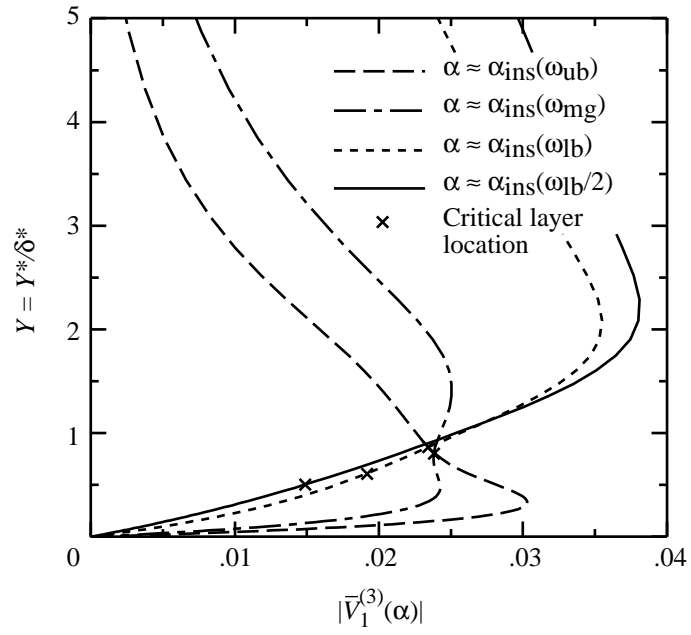


(a)  $\beta = -0.14$ ;  $R_{\delta^*} = 500$ .

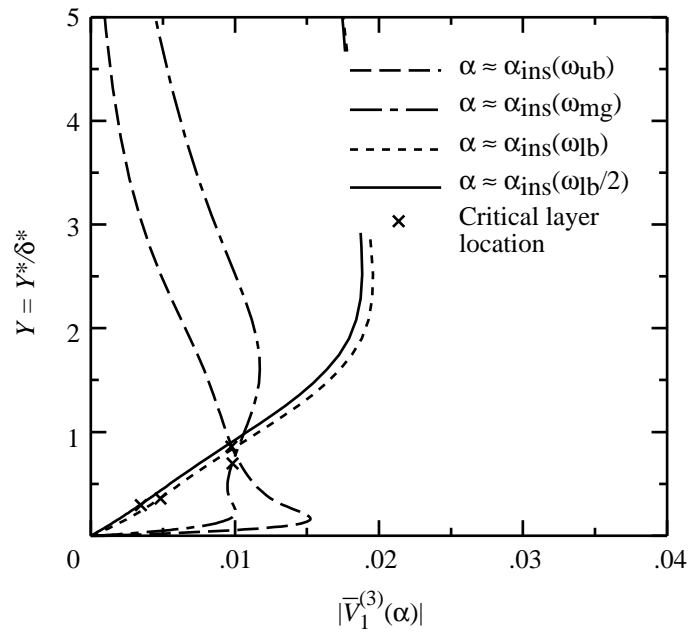


(b)  $\beta = -0.14$ ;  $R_{\delta^*} = 5000$ .

Figure 5. Mean streamwise velocity perturbation produced by wave number  $\alpha$  of wall suction distribution.

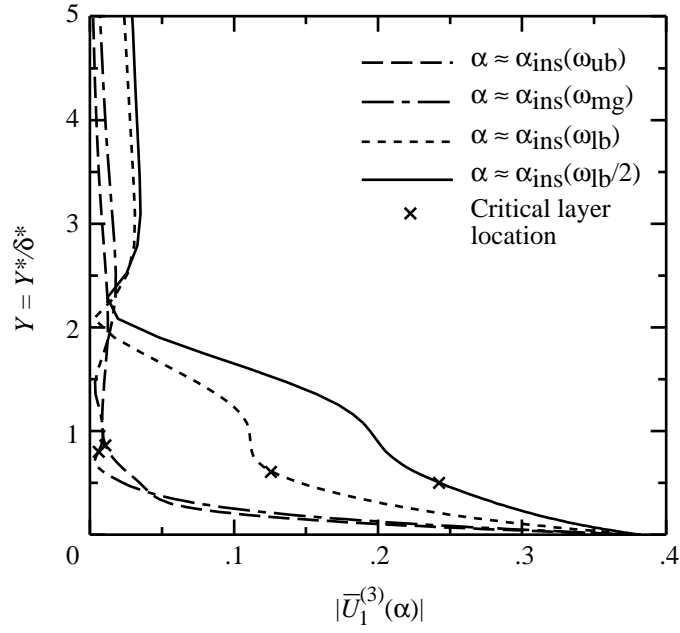


(a)  $\beta = -0.14$ ;  $R_{\delta^*} = 500$ .

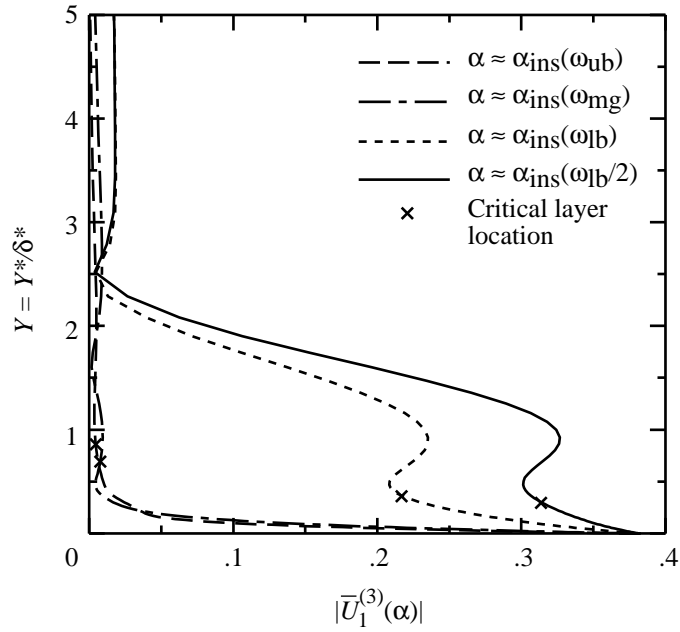


(b)  $\beta = -0.14$ ;  $R_{\delta^*} = 5000$ .

Figure 6. Mean vertical velocity perturbation produced by wave number  $\alpha$  of wall height distribution.

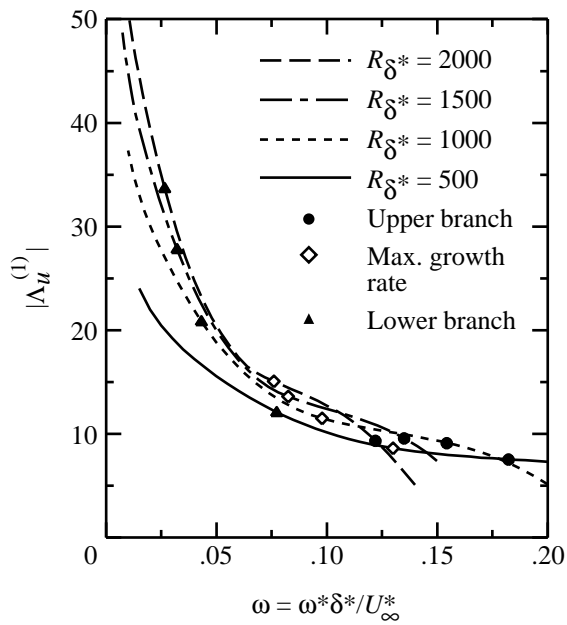


(a)  $\beta = -0.14$ ;  $R_{\delta^*} = 500$ .

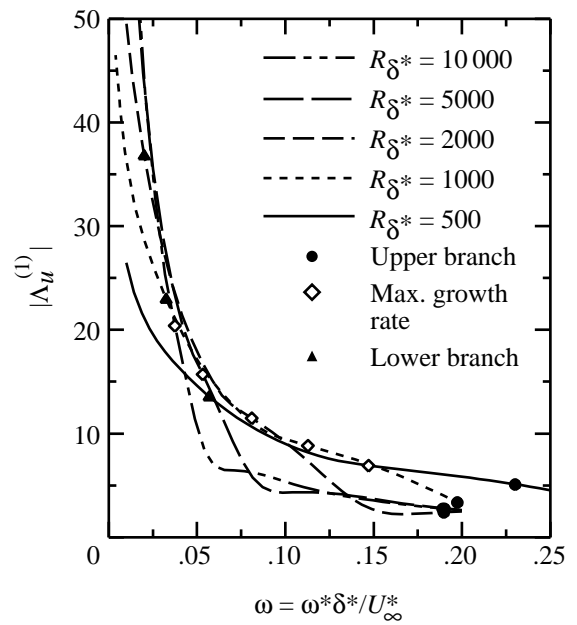


(b)  $\beta = -0.14$ ;  $R_{\delta^*} = 5000$ .

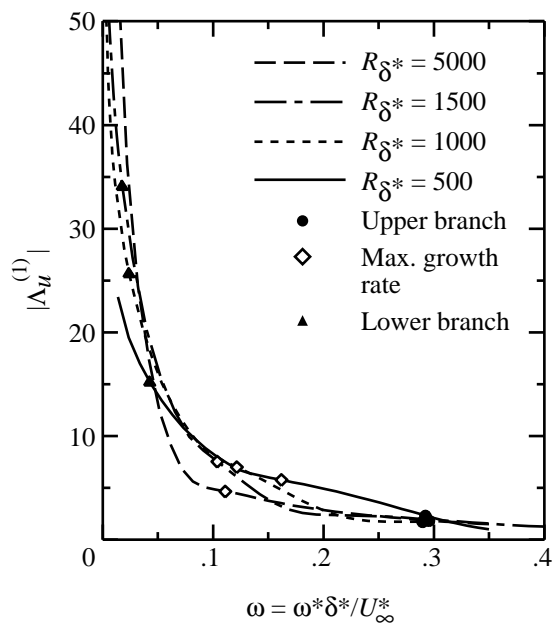
Figure 7. Mean streamwise velocity perturbation produced by wave number  $\alpha$  of wall height distribution.



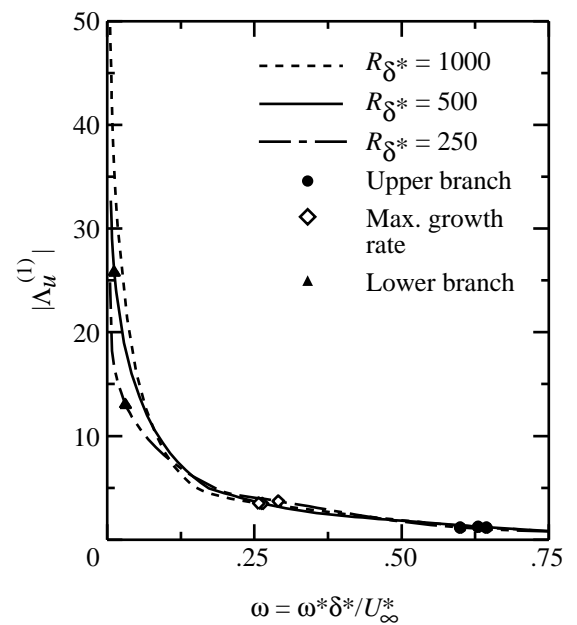
(a)  $\beta = -0.05$ .



(b)  $\beta = -0.10$ .

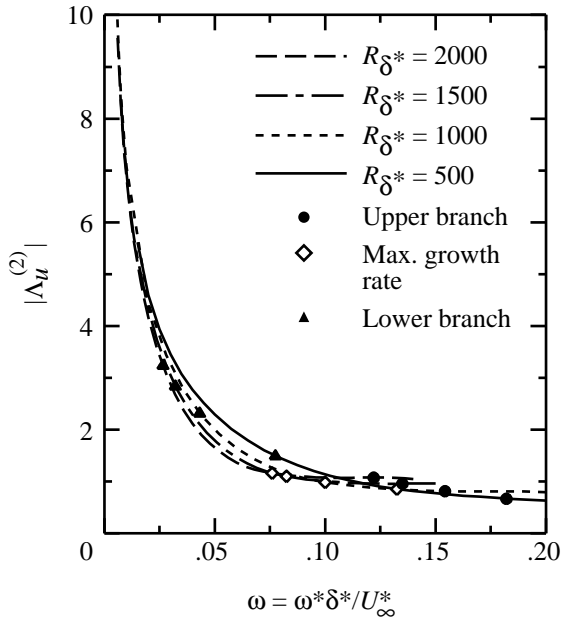


(c)  $\beta = -0.14$ .

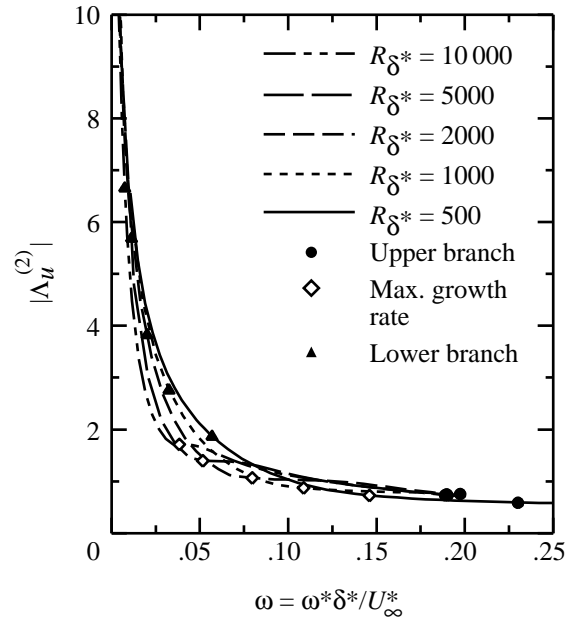


(d)  $\beta = -0.1988$ .

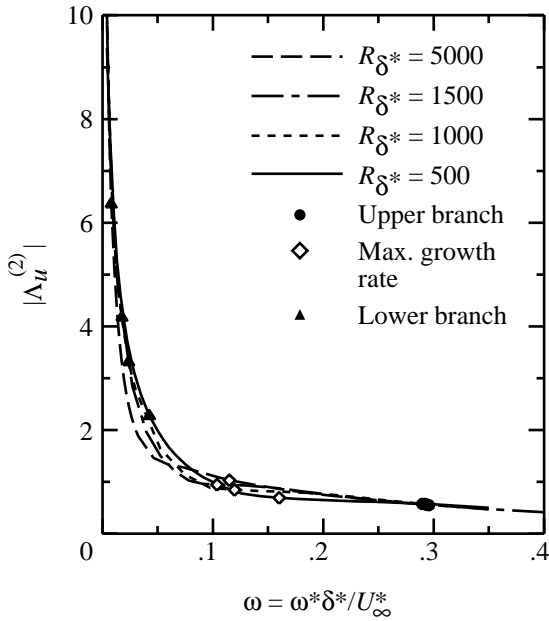
Figure 8. Influence of adverse pressure gradient on efficiency function for wall suction-induced receptivity.



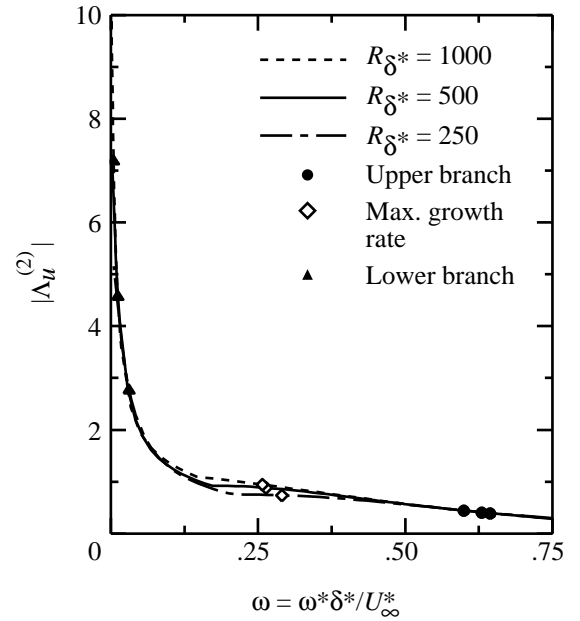
(a)  $\beta = -0.05$ .



(b)  $\beta = -0.10$ .

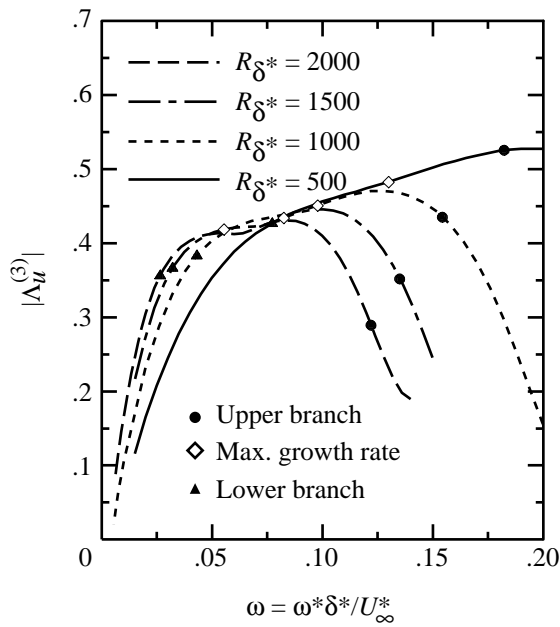


(c)  $\beta = -0.14$ .

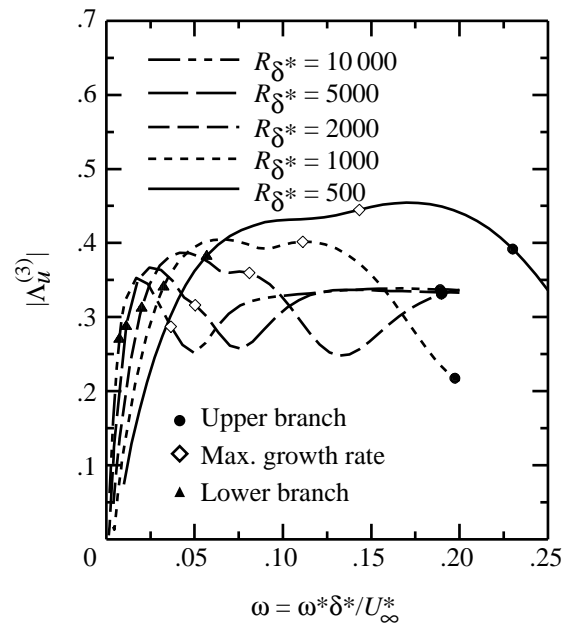


(d)  $\beta = -0.1988$ .

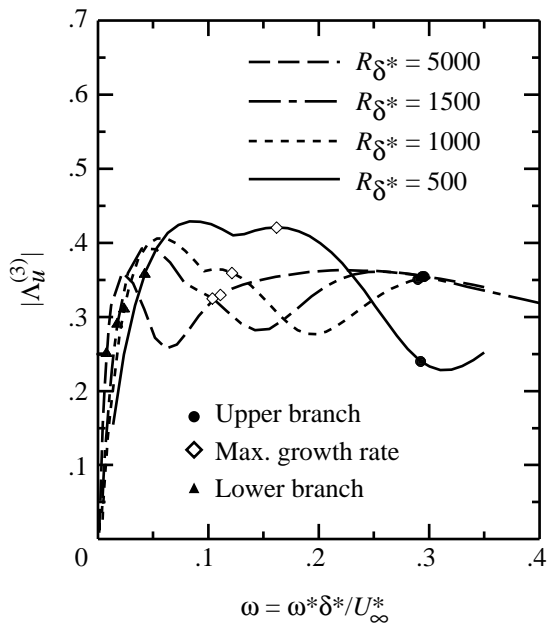
Figure 9. Influence of adverse pressure gradient on efficiency function for wall admittance-induced receptivity.



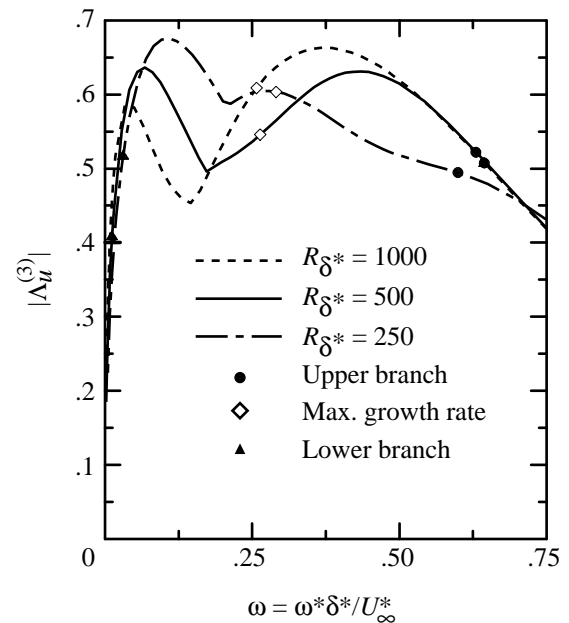
(a)  $\beta = -0.05$ .



(b)  $\beta = -0.10$ .



(c)  $\beta = -0.14$ .



(d)  $\beta = -0.1988$ .

Figure 10. Influence of adverse pressure gradient on efficiency function for wall geometry-induced receptivity.

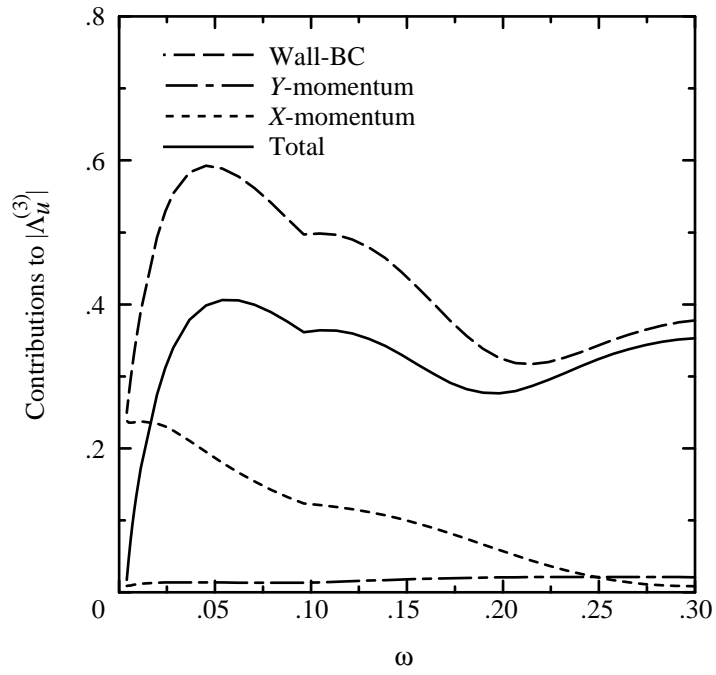
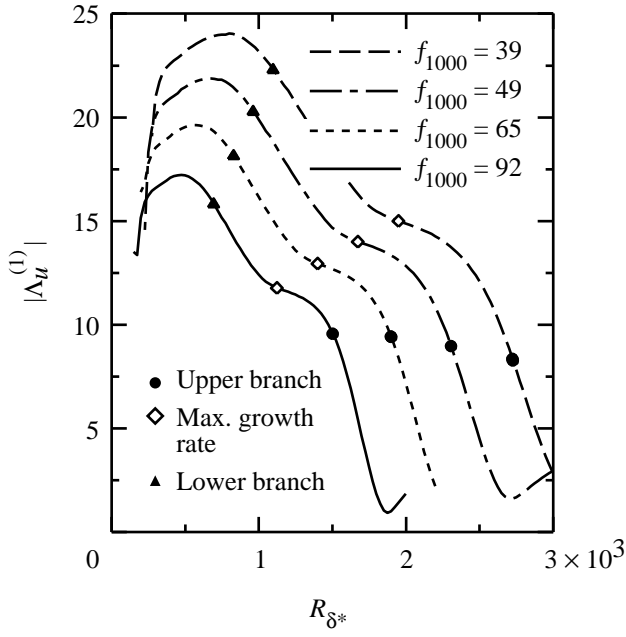
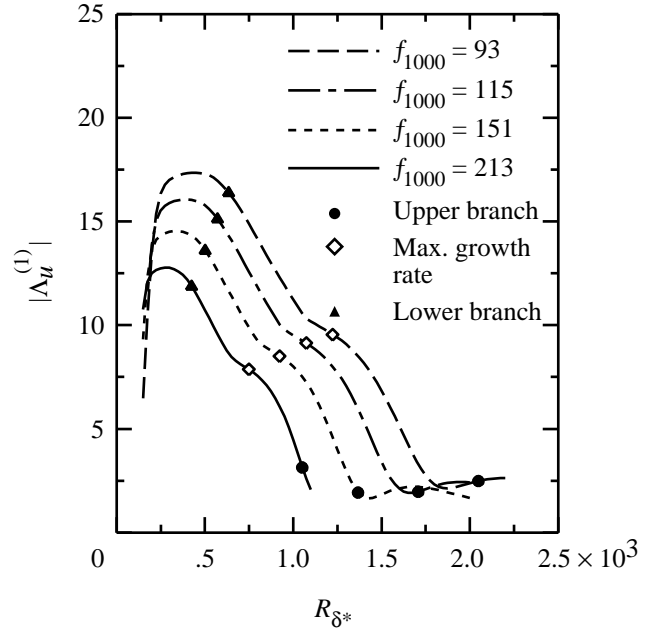


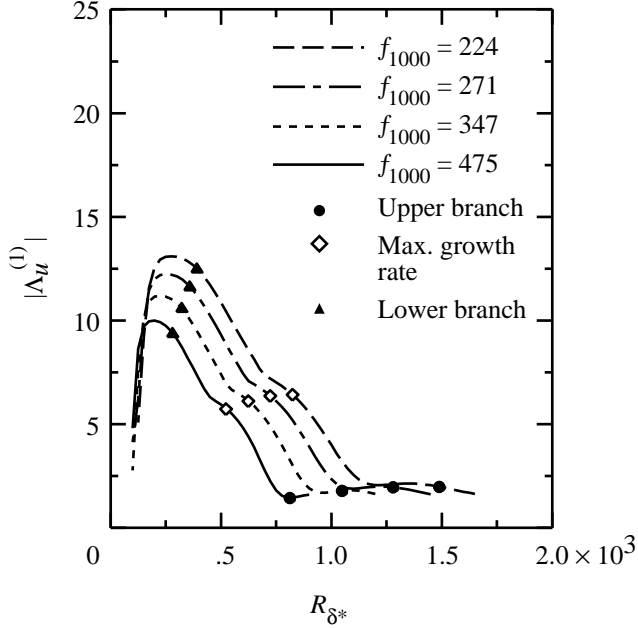
Figure 11. Contributions of inhomogeneous terms in  $X$ - and  $Y$ -momentum equations and inhomogeneous boundary condition (BC) (eq. (3.6b)) to efficiency function for wall geometry-induced receptivity.  $\beta = -0.14$ ;  $R_{\delta^*} = 1000$ .



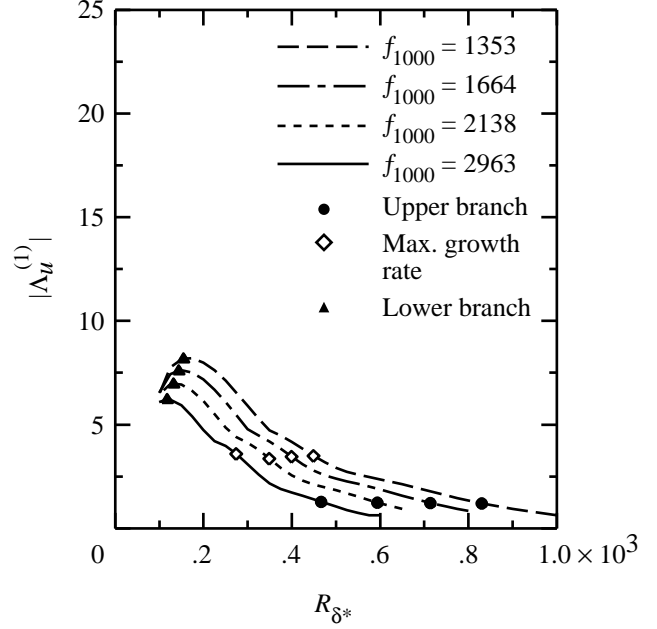
(a)  $\beta = -0.05$ .



(b)  $\beta = -0.10$ .

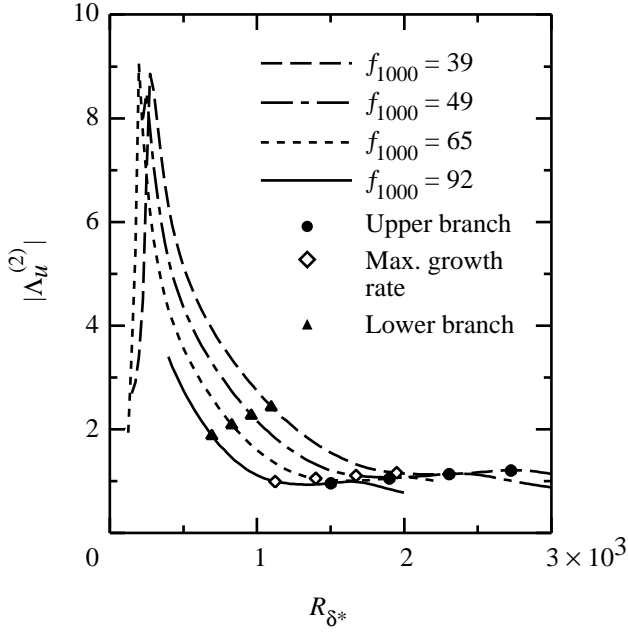


(c)  $\beta = -0.14$ .

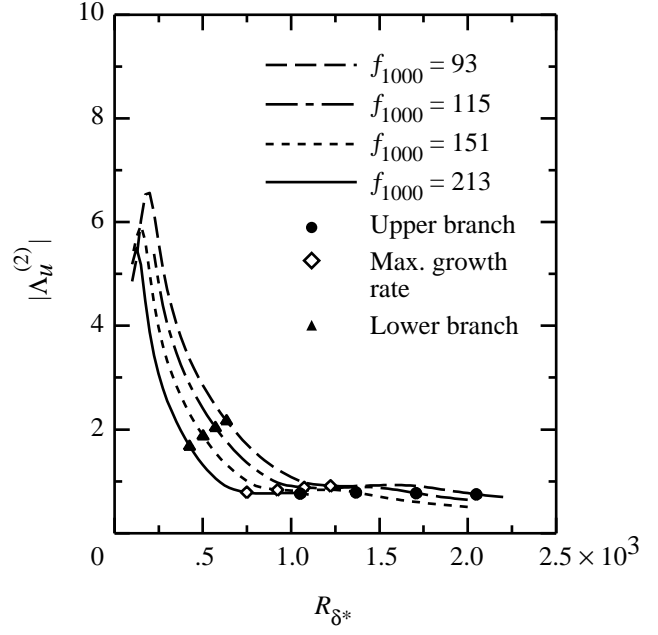


(d)  $\beta = -0.1988$ .

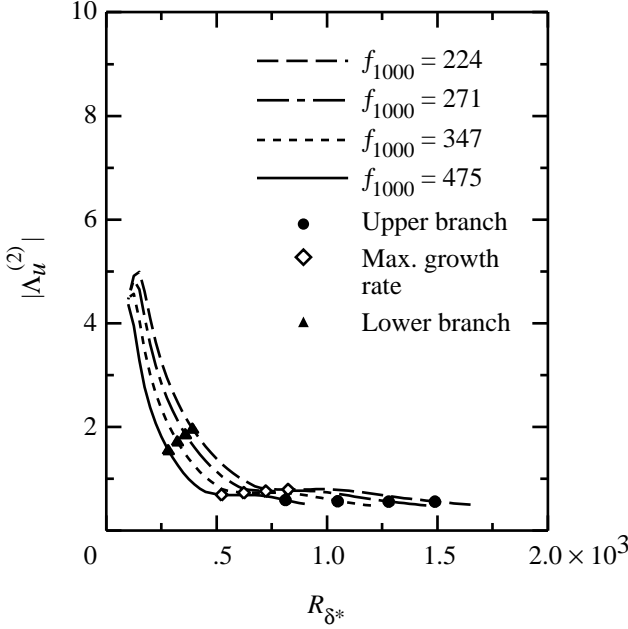
Figure 12. Efficiency function for suction-induced receptivity as a function of wall inhomogeneity location at a fixed acoustic frequency. ( $f_{1000}$  corresponds to nondimensional frequency parameter  $f = \omega^* \nu_\infty^* / U_\infty^{*2}$  at  $R_{\delta^*} = 1000$ .)



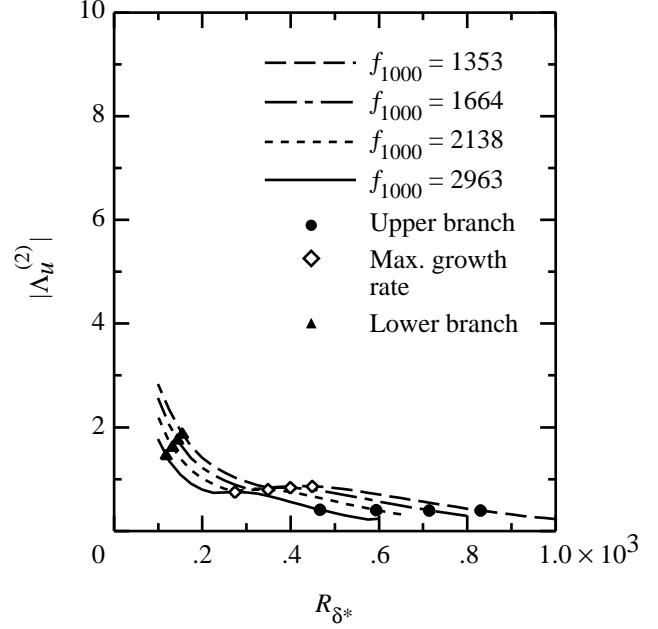
(a)  $\beta = -0.05$ .



(b)  $\beta = -0.10$ .

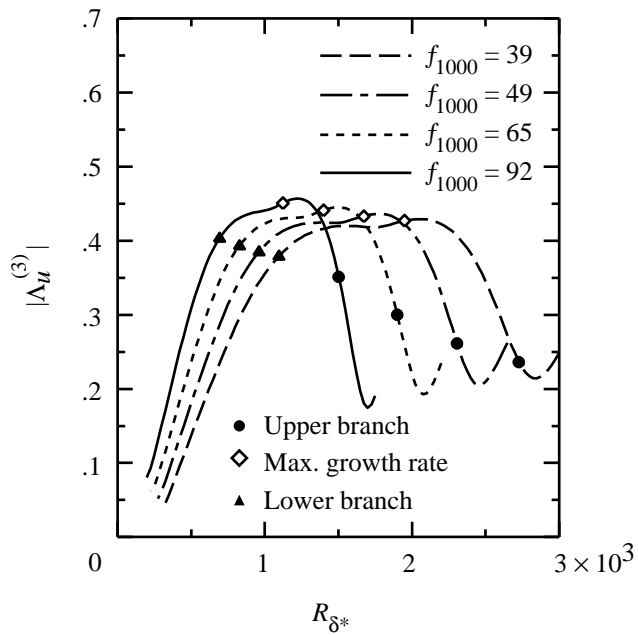


(c)  $\beta = -0.14$ .

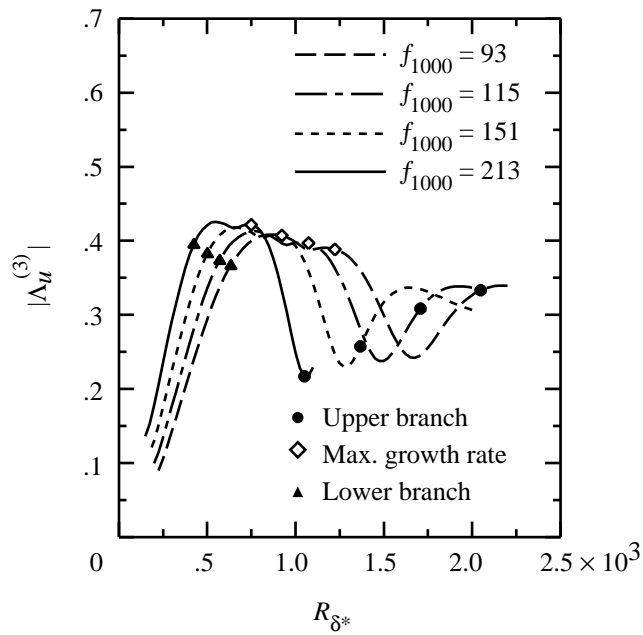


(d)  $\beta = -0.1988$ .

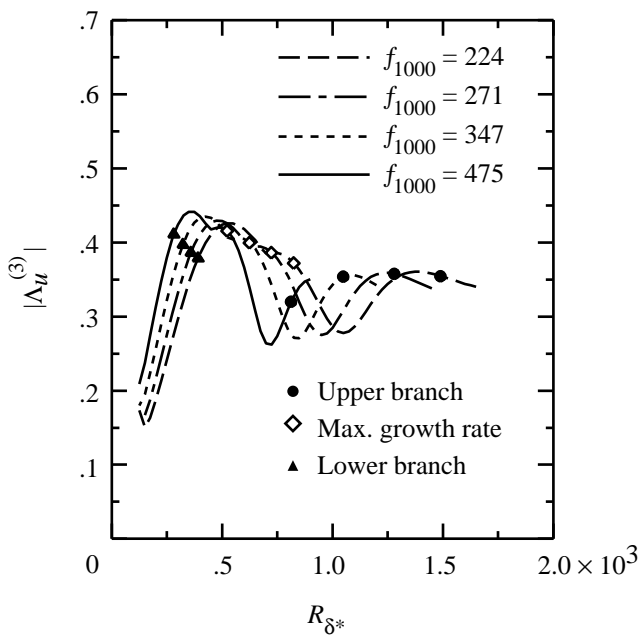
Figure 13. Efficiency function for admittance-induced receptivity as a function of wall inhomogeneity location at a fixed acoustic frequency. ( $f_{1000}$  corresponds to nondimensional frequency parameter  $f = \omega^* \nu_\infty^* / U_\infty^{*2}$  at  $R_{\delta^*} = 1000$ .)



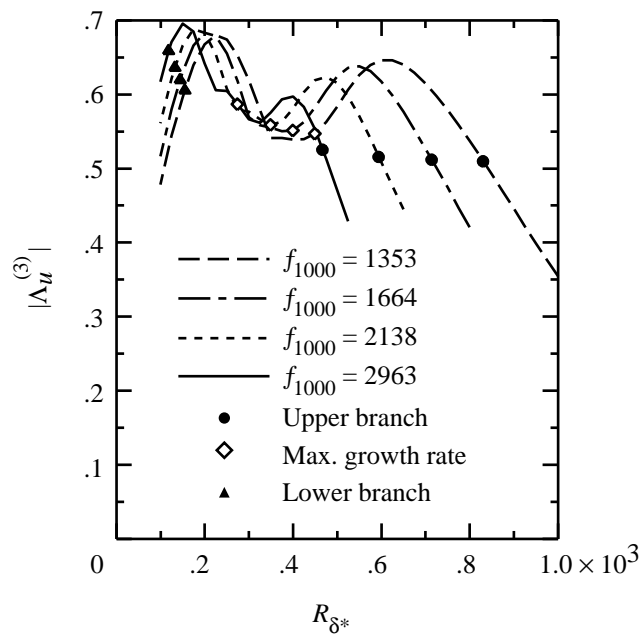
(a)  $\beta = -0.05$ .



(b)  $\beta = -0.10$ .

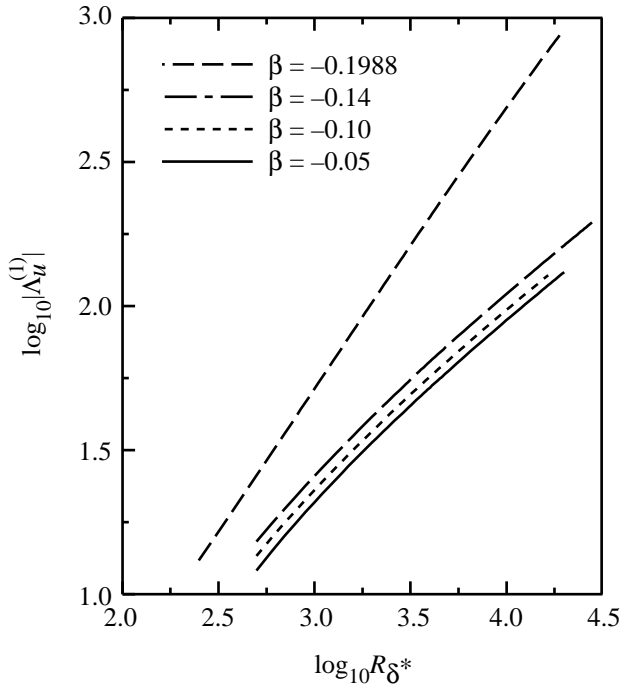


(c)  $\beta = -0.14$ .

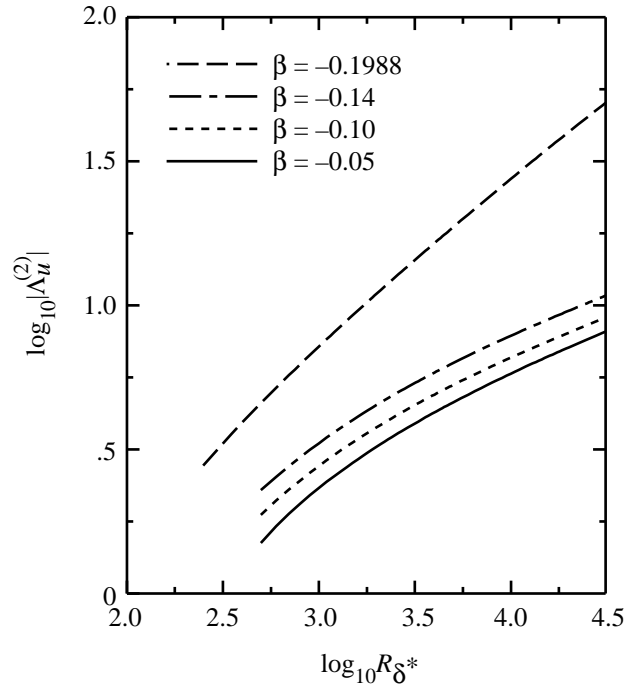


(d)  $\beta = -0.1988$ .

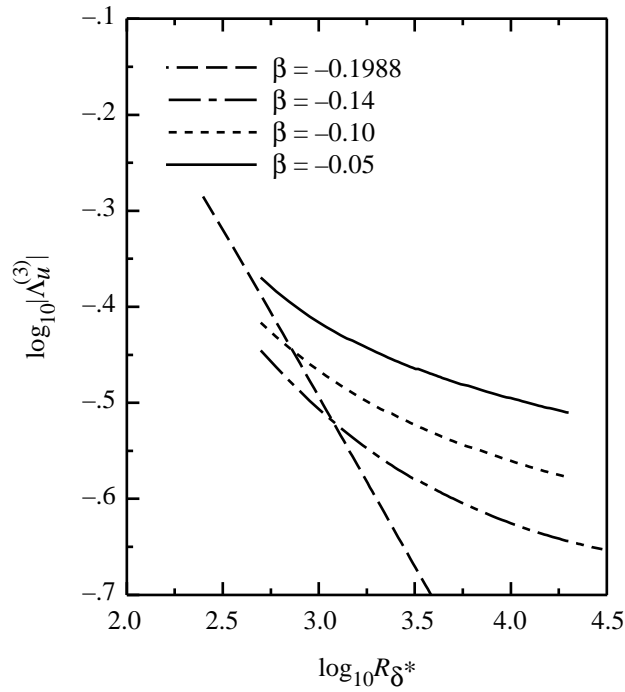
Figure 14. Efficiency function for roughness-induced receptivity as a function of wall inhomogeneity location at a fixed acoustic frequency. ( $f_{1000}$  corresponds to nondimensional frequency parameter  $f = \omega^* \nu_\infty^* / U_\infty^{*2}$  at  $R_{\delta^*} = 1000$ .)



(a) Receptivity due to wall suction variation.



(b) Receptivity due to wall admittance variation.



(c) Receptivity due to wall roughness variation.

Figure 15. Efficiency functions  $|\Lambda_u^{(j)}|$  ( $j = 1, 2, 3$ ) along lower branch of neutral stability curve.

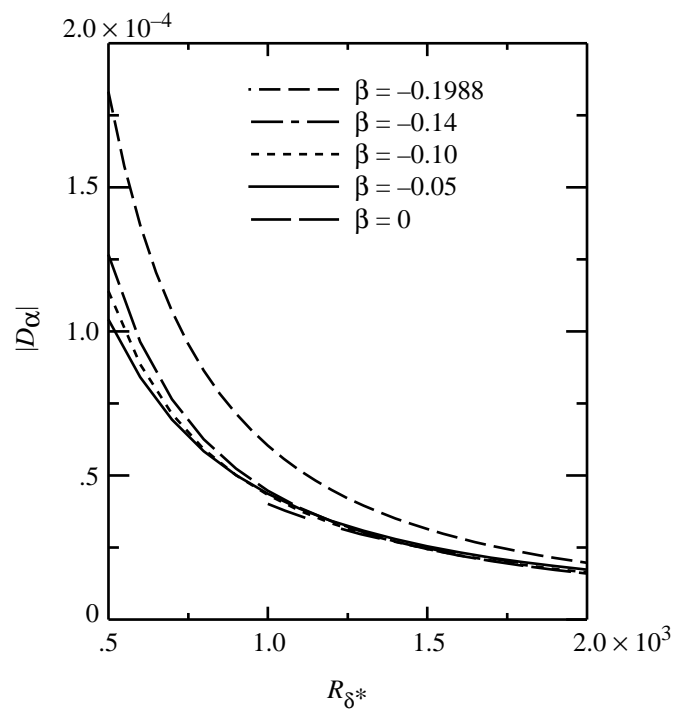
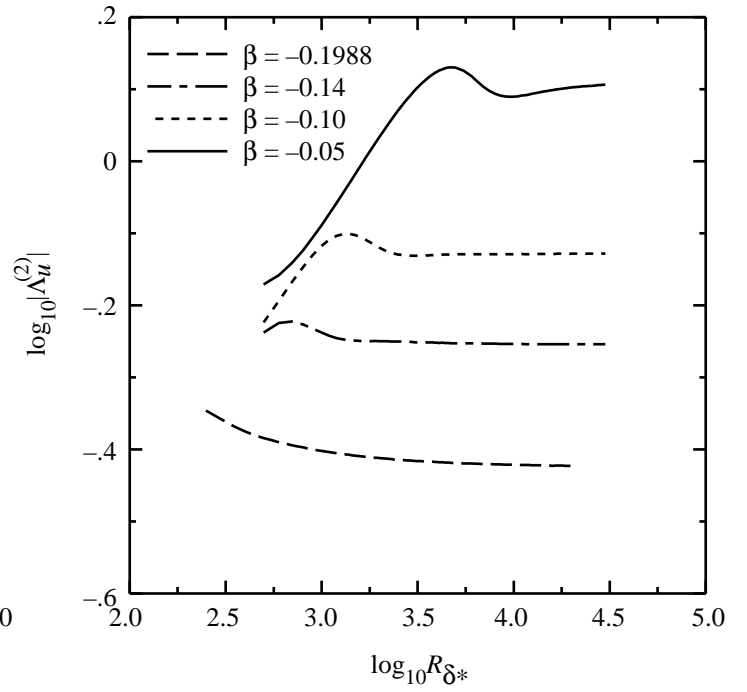
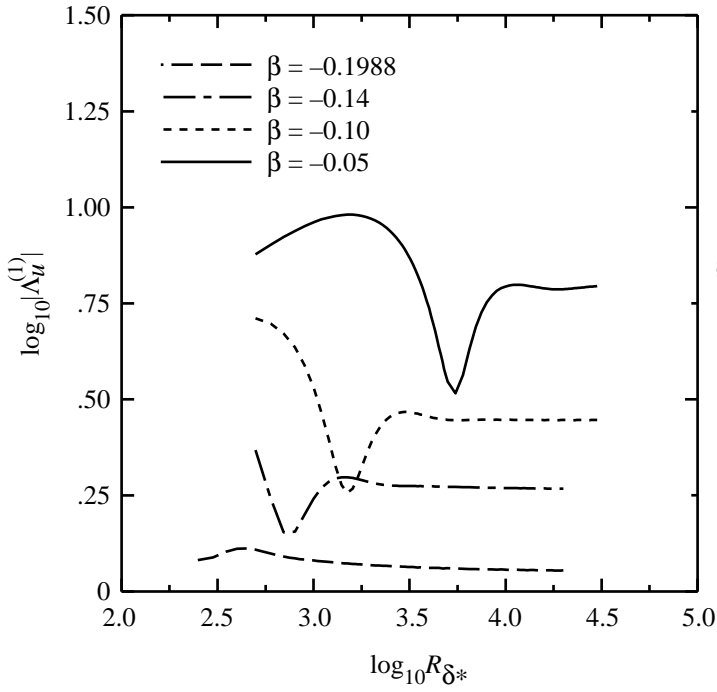
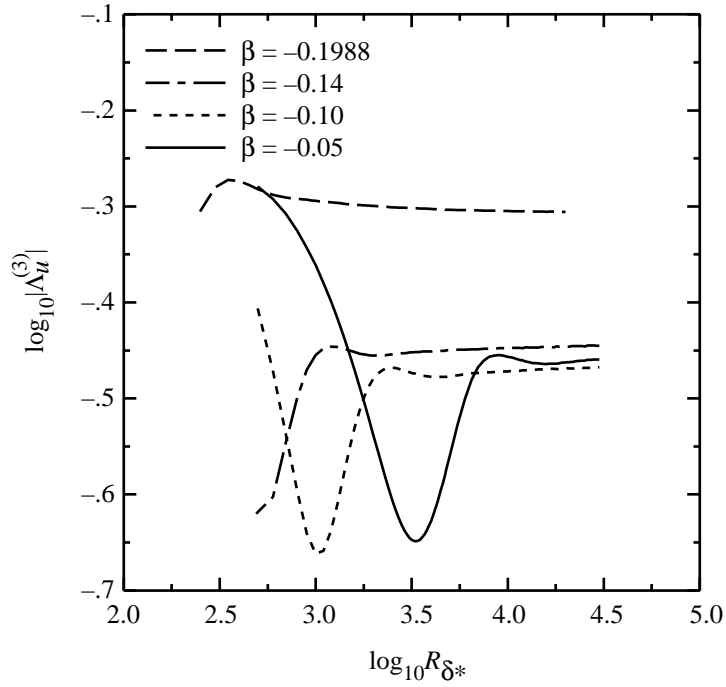


Figure 16. Desynchronization factor  $|D_\alpha|$  versus  $R_{\delta^*}$  at selected values of pressure gradient parameter  $\beta$ .



(a) Receptivity due to wall suction variation.

(b) Receptivity due to wall admittance variation.



(c) Receptivity due to wall roughness variation.

Figure 17. Efficiency functions  $|\Lambda_u^{(j)}|$  ( $j = 1, 2, 3$ ) along upper branch of neutral stability curve.

REPORT DOCUMENTATION PAGE			Form Approved OMB No. 0704-0188	
Public reporting burden for this collection of information is estimated to average 1 hour per response, including the time for reviewing instructions, searching existing data sources, gathering and maintaining the data needed, and completing and reviewing the collection of information. Send comments regarding this burden estimate or any other aspect of this collection of information, including suggestions for reducing this burden, to Washington Headquarters Services, Directorate for Information Operations and Reports, 1215 Jefferson Davis Highway, Suite 1204, Arlington, VA 22202-4302, and to the Office of Management and Budget, Paperwork Reduction Project (0704-0188), Washington, DC 20503.				
1. AGENCY USE ONLY (Leave blank)	2. REPORT DATE February 1995	3. REPORT TYPE AND DATES COVERED Technical Memorandum		
4. TITLE AND SUBTITLE Acoustic Receptivity Due to Weak Surface Inhomogeneities in Adverse Pressure Gradient Boundary Layers			5. FUNDING NUMBERS WU 537-03-23-03	
6. AUTHOR(S) Meelan Choudhari, Lian Ng, and Craig Streett				
7. PERFORMING ORGANIZATION NAME(S) AND ADDRESS(ES) NASA Langley Research Center Hampton, VA 23681-0001			8. PERFORMING ORGANIZATION REPORT NUMBER L-17162	
9. SPONSORING/MONITORING AGENCY NAME(S) AND ADDRESS(ES) National Aeronautics and Space Administration Washington, DC 20546-0001			10. SPONSORING/MONITORING AGENCY REPORT NUMBER NASA TM-4577	
11. SUPPLEMENTARY NOTES Choudhari: High Technology Corporation, Hampton, VA; Ng: Analytical Services & Materials, Inc., Hampton, VA; and Streett: Langley Research Center, Hampton, VA.				
12a. DISTRIBUTION/AVAILABILITY STATEMENT  Unclassified-Unlimited Subject Category 34 Availability: NASA CASI (301) 621-0390			12b. DISTRIBUTION CODE	
13. ABSTRACT (Maximum 200 words) The boundary layer receptivity to free-stream acoustic waves in the presence of localized surface disturbances is studied for the case of incompressible Falkner-Skan flows with adverse pressure gradients. These boundary layers are unstable to both viscous and inviscid (i.e., inflectional) modes, and the finite Reynolds number extension of the Goldstein-Ruban theory provides a convenient method to compare the efficiency of the localized receptivity processes in these two cases. The value of the efficiency function related to the receptivity caused by localized distortions in surface geometry is relatively insensitive to the type of instability mechanism, provided that the same reference length scale is used to normalize the efficiency function for each type of instability. In contrast, when the receptivity is induced by variations in wall suction velocity or in wall admittance distribution, the magnitudes of the related efficiency functions, as well as the resulting coupling coefficients, are smaller for inflectional (i.e., Rayleigh) modes than for the viscous Tollmien-Schlichting waves. The reduced levels of receptivity can be attributed mainly to the shorter wavelengths and higher frequencies of the inflectional modes. Because the most critical band of frequencies shifts toward higher values, the overall efficiency of the wall suction- and wall admittance-induced receptivity decreases with an increase in the adverse pressure gradient.				
14. SUBJECT TERMS Laminar boundary layers; Transition; Boundary layer receptivity; Falkner-Skan boundary layers; Tollmien-Schlichting waves; Rayleigh modes			15. NUMBER OF PAGES 36	
			16. PRICE CODE A03	
17. SECURITY CLASSIFICATION OF REPORT Unclassified	18. SECURITY CLASSIFICATION OF THIS PAGE Unclassified	19. SECURITY CLASSIFICATION OF ABSTRACT Unclassified	20. LIMITATION OF ABSTRACT	